Int J Fract (2026) 250:6
https://doi.org/10.1007/s10704-025-00901-y

RESEARCH

Damage-mechanics insights into the relationship between upper-shelf Charpy testing and J-integral testing considering varying tensile test properties

Wei Jun Wong · Carey L. Walters

Received: 18 June 2025 / Revised: 6 December 2025 / Accepted: 11 December 2025

Abstract Requirements on the yield-to-tensile strength ratio σ_y/σ_u, fracture elongation A and the Charpy energy C_v are used together as part of an indirect method of ensuring sufficient ductility at localised areas of stress and strain concentration in the design of steel structures. Recent studies have found that these indirect requirements could be inadequate in certain situations involving cracks or manufacturing defects. Furthermore, requirements on the σ_y/σ_u which are enforced regardless of the structural context and other material properties may unnecessarily constrain the use of steels which nonetheless have high strength, fracture toughness and ductility. In contrast to the σ_y/σ_u, A, and C_v, a more direct measurement of a structure's ability to resist fracture is given by fracture toughness testing, such as J-integral testing, but this is less frequently used, because these tests are significantly costlier than tension and Charpy tests. More often, Charpy tests are performed and correlations between upper-shelf C_v and J values are used to estimate the fracture toughness of the material. However, the existing correlations are predominantly based on empirical findings and have not systematically accounted for the effect of variations in the σ_y/σ_u, which has been shown in recent studies to affect the fracture toughness. Using a previously validated coupled damage-mechanics model with rate- and temperature-dependent plasticity and damage softening, this paper investigates the correlation between C_v and J_Q (the critical J) numerically, including how it is affected by other material certificate properties such as the σ_y/σ_u and A. First, a correlation based on regression between the damage parameters and the mechanical properties from mill test certificates is found by calibrating the damage parameters for a large database of these steels. Then, the correlation between C_v and J_Q is assessed by simulating the single-edge-notch bending test for a range of varying mill test certificate properties, taking into account how the damage parameters vary with these mechanical properties. The results are analysed to give better insight into how the notch toughness correlates to the fracture toughness, taking the σ_y/σ_u and A into account. It is seen that although varying σ_y/σ_u and A has some effect on how the total notch energy C_v is correlated to J_Q, it does not reflect a significant effect on the ductile fracture initiation toughness but is rather associated with the fact that the C_v includes a significant portion of energy for stable ductile propagation and fracture occurring at the specimen's free surface, while J_Q primarily concerns the onset stage of stable ductile tunnelling behaviour at the centre of the specimen. The σ_y/σ_u and A are seen to have an even smaller effect on the correlation between J_Q and the energy (C_{vm}) dissipated up to the occurrence of the peak force in the instrumented Charpy test, in comparison with the C_v–to–J_Q correlation, especially for low C_{vm}.

W. J. Wong (✉) · C. L. Walters
Department of Maritime and Transport Technology, Delft University of Technology, Mekelweg 2, 2628 CD Delft, South Holland, The Netherlands
e-mail: w.j.wong@tudelft.nl

Published online: 11 January 2026

Keywords Consistency model · High-strength steel · Mill test report · Modified Mohr-Coulomb · Notch energy · Viscoplasticity

List of symbols

A_ε	Engineering strain at full fracture in tensile test
A	Fracture elongation over the proportional gauge length from pieced-together tensile test fragments
Δa	Crack extension
C	Cowper-Symonds coefficient
C_1	Normalised MMC parameter relating to the strain in the MMC surface when $c_1 = 0$; $\eta = 2.5$; $\bar{\theta} = 0$
C_2	Normalised MMC parameter relating to the maximum strain in the MMC surface when $c_1 = 0$
C_3	Normalised MMC parameter relating to the minimum strain in the MMC surface when $c_1 = 0$
c	Specific heat capacity
c_1	First MMC strain surface parameter
c_2	Second MMC strain surface parameter
c_3	Third MMC strain surface parameter
C_v	Charpy V-notch energy
C_{vm}	Portion of the Charpy energy dissipated before the peak in the force-displacement plot from the instrumented Charpy test
D	Damage indicator
D_c	Critical damage
$\mathcal{D}_p$	Internal woryhyhk due to plastic deformation
E	Young's modulus
e	Euler's number
f	Yield function
g	Average slope for Swift hardening in the true stress versus true plastic strain space, between $\varepsilon_{sh,p}$ and $\varepsilon_{u,p}$
g_H	Average slope for Hollomon hardening rule in the true stress versus true total strain space, between $\varepsilon_{y,t}$ and $\varepsilon_{u,t}$
J	J-integral
$J_{1\,\mathrm{mm},S}$	J at 1mm crack extension according to Schindler's (2001) conversion from Charpy testing
$J_{1\,\mathrm{mm},W}$	J at 1mm crack extension according to Wallin's (2001) conversion from Charpy testing
J_Q	Critical J based on the 0.2 mm crack extension offset
J_{QS}	Critical J based on the 0.2 mm crack extension offset using the Schindler (2001) conversion from Charpy energy
J_{QW}	Critical J based on the 0.2 mm crack extension offset using the Wallin (2001) conversion from Charpy energy
K	Strength coefficient for Swift the hardening power law
K_H	Strength coefficient for the Hollomon hardening power law
l_c	Characteristic element length
m	Damage softening exponent
m_S	Schindler J-Δa curve exponent
m_W	Wallin J-Δa curve exponent
m_x	Thermal softening exponent
n	Strain hardening exponent for the Swift hardening power law
n_H	Strain hardening exponent for the Hollomon hardening power law
P	Fitting parameters for the regression of C_v on C_2, C_3 and σ_y/σ_u
Q	Fitting parameters for the regression of A on C_2 and C_3
q	Cowper-Symonds exponent
R	Rate-dependence factor
X	Thermal softening factor
Z	Parameter for the grouped effect of the MMC c_1 terms when $\eta = 2.5$; $\bar{\theta} = 0$
β	Softening coefficient
ε_0	Swift offset strain
ε_f	Ductile damage initiation strain
ε_p	Equivalent plastic strain
$\dot{\varepsilon}_p$	Equivalent plastic strain rate
$\dot{\varepsilon}_{p0}$	Equivalent plastic strain rate offset parameter
$\dot{\varepsilon}_{p,uni}$	Quasi-static-uniaxial-testing equivalent plastic strain rate parameter
$\ddot{\varepsilon}_p$	Rate of change of the plastic strain rate
ε_{sh}	Total engineering strain corresponding to the end of the yield plateau
$\varepsilon_{sh,p}$	Equivalent plastic strain corresponding to the end of the yield plateau
ε_u	Uniform elongation, i.e. the engineering strain at the onset of necking
$\varepsilon_{u,p}$	Equivalent plastic strain corresponding to the occurrence of necking instability
$\varepsilon_{u,t}$	True total strain at the occurrence of necking instability

$\dot{\boldsymbol{\varepsilon}}_{\boldsymbol{vp}}$	Viscoplastic strain rate tensor
$\varepsilon_{y,t}$	True total strain at the initial yield point
η	Stress triaxiality
Θ	Temperature
Θ_m	Melting temperature
Θ_r	Room temperature
$\bar{\theta}$	Normalised Lode angle
ν	Poisson's ratio
ξ	Chatterjee correlation coefficient
ρ	Density
$\bar{\sigma}$	Quasi-static undamaged stress due to plastic strain hardening only
σ_{fS}	Average flow stress according to Schindler (2001)
σ_{fW}	Average flow stress according to Wallin (2001)
σ_u	Ultimate tensile stress from uniaxial tensile test
σ_v	von Mises equivalent stress
σ_y	Yield strength from uniaxial tensile test
$\sigma_{y,cold}$	Estimated initial flow stress at at low temperature
$\sigma_{y,room}$	Initial flow stress at room temperature
$\boldsymbol{\sigma}$	Cauchy stress tensor
χ	Taylor-Quinney energy coefficient
FEA	Finite-element analysis
MMC	Modified Mohr-Coulomb
SENB	Single-edge notched bending

1 Introduction

Structural details such as corners, holes, cut-outs, welded connections and notches are geometrical stress raisers that often experience plastic strains even before the yielding limit state of the global, structural-level member is reached. Ductility is required in these areas to allow the redistribution of these stresses and to maintain the local load bearing capacity, which is sometimes also worsened by fatigue-induced cracks or manufacturing defects. In many steel design standards (CEN 2005, 2020; AISC 2022) and maritime classification rules (LR 2024; DNV 2021), it is implied that complying with a maximum limit on the yield-to-tensile strength ratio σ_y/σ_u, a minimum required fracture elongation A and a minimum transition-temperature-based Charpy notch energy C_v is sufficient to ensure that the ductile fracture behaviour and strength assumed in the ultimate strength design calculations can be achieved and maintained at these locations (Feldmann et al. 2020). The σ_y/σ_u limit amounts to a minimum strain hardening requirement that serves to delay necking (Considère 1885; Wong and Walters 2021), which causes the occurrence of large strains leading to fracture. The minimum fracture elongation A is a provision for delaying low-triaxiality ductile fracture (Feldmann and Schaffrath 2017). The transition-temperature-based minimum Charpy energy C_v is a provision for the avoidance of brittle fracture behaviour (Feldmann et al. 2020). In this way, these requirements are considered to act as an indirect substitute for an upper-shelf toughness requirement that has not been explicitly specified in the design codes and rules.

Recent studies (Feldmann et al. 2020; Sedlacek et al. 2008) have found that this set of indirect requirements could be inadequate for providing sufficient upper-shelf toughness in certain situations involving cracks or manufacturing defects. On the other hand, fixed requirements on the σ_y/σ_u which are enforced regardless of the structural context and other properties may, in some situations, unduly constrain the use of steels which nonetheless have high strength, fracture toughness and ductility (Feldmann et al. 2023; Feldmann and Schaffrath 2017). It is found that strain hardening, as represented by the σ_y/σ_u, has a significant effect on the ductility in plastic buckling mechanisms (Wong and Walters 2023; Studer and Taras 2023), but its effect on the local ductility at stress-concentration-inducing details is less clear (Langenberg et al. 2000). While a maximum σ_y/σ_u limit of 0.95 was indeed initially introduced (Dhalla and Winter 1974) based on the grounds of delaying necking sufficiently to ensure a minimum level of ductility, and similar values for the σ_y/σ_u limit are used to this day, post-necking behaviour and fracture toughness were neglected in these considerations. More comprehensive research on the effect of strain hardening on local ductility at cracked details under positive triaxiality is ongoing, but the implications thereof on the use of σ_y/σ_u as an indicator of local ductility at such details lack a consensus. For example, Feldmann et al. (2020) and Feldmann and Schaffrath (2017) indicate that a higher σ_y/σ_u leads to increased net section resistance relative to the ultimate tensile strength in centrally notched tensile tests, suggesting that a higher σ_y/σ_u promotes resistance at cracked details. On the other hand, Nonn et al. (2018) and Lu et al. (2015) indicate that a higher σ_y/σ_u leads to

decreased crack arrest toughness, suggesting the contrary.

In light of this, recent developments have seen the suggestion of minimum upper-shelf C_v values (CEN 2023), in addition to A, as a better primary upper-shelf toughness substitute criterion, while maintaining a minimal σ_y/σ_u for the ductility at plastic buckling localisations and the provision of a nominal minimum hardening so that plastic mechanisms can develop (Feldmann et al. 2023). Although ductile Charpy tests, when compared to fracture toughness tests, are additionally affected by strain rate effects and adiabatic heating and are more influenced by plastic energy dissipation due to extensive plastic bending, they are cheaper and easier to perform. Correlations between the upper-shelf notch toughness in terms of C_v and the fracture toughness in terms of the J-integral are often used to estimate the material's fracture toughness from Charpy tests (Wallin 2001; BSI 2019; Chaouadi and Gérard 2021). These correlations provide the basis for the the use of minimum upper-shelf C_v values as an indirect upper-shelf toughness requirement for local ductility at details susceptible to crack formation and ultimate ductile fracture.

The existing correlations, however, are predominantly based on empirical findings and have not systematically accounted for the effect of variations in the σ_y/σ_u on the toughness noted by Nonn et al. (2018) and Lu et al. (2015). Only one existing semi-empirical correlation, proposed by Schindler (2001), which will be discussed in Section 4 below, varies with σ_y/σ_u. Relationships based on damage-plasticity modelling do not exist in the literature primarily because calibrating such models to capture the ductile fracture mechanism well for even one material alone typically involves extensive testing and numerical modelling effort (Cao 2015). Recently, a study on the modelling of the Charpy and single-edge-notched-bending (SENB) tests on AH36 and S690QL steel by the present authors (Wong and Walters 2025) has shown that, for steels with weak triaxiality dependence in the fracture locus, these two tests could be simulated well using a 2-parameter approach for the damage locus calibration, by assuming triaxiality independence. This is supported by observations made by Xue (2009, 2010) on existing experiments on structural steels (Clausing 1970) and aluminium alloy (Banabic et al. 2005). By virtue of the reduced calibration effort given by this approach, this paper numerically investigates the correlation between C_v and the critical J, denoted by J_Q, predicted by the calibrated models of a database of S690Q (CEN 2019) steels. The calibration is performed based on the data obtained from the material certificate of these steels: σ_y, σ_u, A and C_v. Using regression analysis of the numerical results, a relationship between the damage parameters and material certificate data is proposed for this group of steels. Subsequently, SENB simulations, together with the corresponding J_Q, for the calibrated steels with varying material certificate properties are obtained. The results are analysed to study and give better insight into how the notch toughness C_v correlates to the fracture toughness J_Q, taking the σ_y/σ_u and A into account. This sheds light on the roles of σ_y/σ_u and A in the local ductility at cracked details under positive triaxiality by revealing how they affect the way notch and fracture toughness measures are correlated, presenting quantified effects of σ_y/σ_u and A on fracture toughness considerations.

2 Rate- and temperature-dependent damage-softening plasticity model

A rate- and temperature-dependent damage-softening flow plasticity model, as described by Wong and Walters (2025), is used. The effects are coupled multiplicatively in the yield function shown in Eq. (1), which is solved by using the consistency viscoplasticity formulation by Wang et al. (1997).

$$f = \sigma_v - \bar{\sigma} R \beta X \tag{1}$$

where f is the yield function; σ_v is the von Mises equivalent stress; $\bar{\sigma}$ is the plastic strain-hardening stress; R is the rate-dependence factor; β is the softening coefficient; and X is the thermal softening factor.

2.1 Plasticity

The plastic strain-hardening stress $\bar{\sigma}$ is described by a Swift-type (Swift 1952) stress-strain curve combined with a yield plateau:

$$\bar{\sigma} = \begin{cases} \sigma_y \left(\dfrac{\varepsilon_{sh} - \dfrac{\sigma_y}{E}}{\varepsilon_{sh,p}} \varepsilon_p + \dfrac{\sigma_y}{E} + 1 \right) & 0 < \varepsilon_p < \varepsilon_{sh,p} \\ K(\varepsilon_p - \varepsilon_0)^n & \varepsilon_p \geq \varepsilon_{sh,p} \end{cases} \tag{2}$$

$$\varepsilon_{sh,p} = \ln(1 + \varepsilon_{sh}) - \ln\left(1 + \frac{\sigma_y}{E}\right) \tag{3}$$

where ε_p is the true equivalent plastic strain; ε_{sh} and $\varepsilon_{sh,p}$ are respectively the total engineering strain and the true equivalent plastic strain corresponding to the end of the yield plateau; K is the strength coefficient; n is the strain hardening exponent; and ε_0 is the Swift offset parameter.

The Young's modulus E, which is very similar for most structural steels, is here assumed to be 200 GPa (together with a Poisson's ratio of 0.3). The ε_{sh} and ε_u are obtained from the relationships proposed by Yun and Gardner (2017), derived from from regression analysis of 455 engineering stress-strain curves of structural hot-rolled steels with nominal grades up to S690, as shown in Eqs. (4) and (5):

$$\varepsilon_{sh} = \begin{cases} 0.0015 & \dfrac{\sigma_y}{\sigma_u} < 0.7 \\ 0.1\dfrac{\sigma_y}{\sigma_u} - 0.055 & 0.7 \leq \dfrac{\sigma_y}{\sigma_u} \leq 0.85 \\ 0.03 & \dfrac{\sigma_y}{\sigma_u} > 0.85 \end{cases} \tag{4}$$

$$\varepsilon_u = \begin{cases} 0.6\left(1 - \frac{\sigma_y}{\sigma_u}\right) & \frac{\sigma_y}{\sigma_u} \leq 0.9 \\ 0.06 & \frac{\sigma_y}{\sigma_u} > 0.9 \end{cases} \tag{5}$$

Given the known values above, assuming that the occurrence of the ultimate tensile strength σ_u and the associated uniform elongation ε_u satisfies the Considère (1885) criterion for necking and that the Swift power hardening curve intersects the yield plateau at $\varepsilon_p = \varepsilon_{sh,p}$ enables the remaining parameters K, n, ε_0 to be solved for. Thus, an estimate of the plastic strain hardening curve can be found from the σ_y and σ_u available from a material certificate.

2.2 Strain-rate dependence

The rate-dependence factor R is described by a Cowper-Symonds-type (Cowper and Symonds 1957) relation:

$$R = 1 - \left(\frac{\dot{\varepsilon}_{p,uni} + \dot{\varepsilon}_{p0}}{C}\right)^{\frac{1}{q}} + \left(\frac{\dot{\varepsilon}_p + \dot{\varepsilon}_{p0}}{C}\right)^{\frac{1}{q}} \tag{6}$$

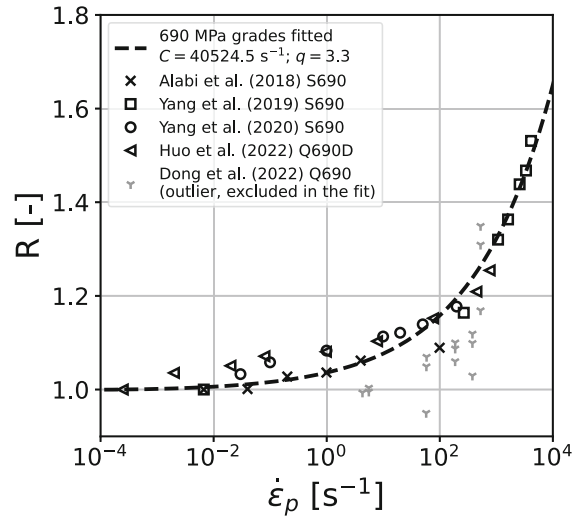

Fig. 1 Least-squares fit of R and experiments in the literature (Alabi et al. 2018; Yang et al. 2019, 2020; Huo et al. 2022; Dong et al. 2022)

where C is the Cowper-Symonds coefficient; and q is the Cowper-Symonds exponent; $\dot{\varepsilon}_p$ is the equivalent plastic strain rate; $\dot{\varepsilon}_{p,uni}$ is the quasi-static-uniaxial-testing equivalent plastic strain rate; and $\dot{\varepsilon}_{p0}$ is the equivalent plastic strain rate offset parameter which serves to ensure that the gradient of R with respect to $\dot{\varepsilon}_p$ is finite when $\dot{\varepsilon}_p = 0$ as needed for convergence in the solution of the yield function (Eq. (1)), unlike in the original Cowper-Symonds equation where it is infinite.

Both the $\dot{\varepsilon}_{p,uni}$ and $\dot{\varepsilon}_{p0}$ are here assumed to be 0.00025 s^{-1}, the uniaxial testing rate according to ISO 6892-1 (ISO 2019). C and q are assumed to be 40524.5 s^{-1} and 3.3, respectively, based on least-squares fitting to existing experimental data in the literature (Alabi et al. 2018; Yang et al. 2019, 2020; Huo et al. 2022), as shown in Fig. 1. The data from Dong et al. (2022) was not included in the fit due to its nature as an outlier in comparison to the data cloud formed by the rest of the experiments.

2.3 Thermal softening

The thermal softening factor X is based on that of the Johnson-Cook (Johnson and Cook 1985) plasticity model:

$$X = 1 - \left(\frac{\Theta - \Theta_r}{\Theta_m - \Theta_r}\right)^{m_x} \tag{7}$$

where Θ is the temperature, Θ_m is the melting temperature, Θ_r is the room temperature, and m_x is the thermal softening exponent.

In the Charpy simulations, in which accounting for thermal softening effects is important (Tanguy et al. 2005; Seo et al. 2024) especially when C_v is high (Wong and Walters 2025), adiabatic conditions are assumed, such that the energy dissipated due to plastic deformation leads to an increase in the temperature of the material, according to the relationships given in Eqs. (8) and (9):

$$\dot{\mathcal{D}}_p = \frac{\boldsymbol{\sigma} : \dot{\boldsymbol{\varepsilon}}_{\boldsymbol{vp}}}{\rho} \tag{8}$$

where $\dot{\mathcal{D}}_p$ is the rate of internal work done attributed to plastic deformation (Besseling and van der Giessen 1994); $\boldsymbol{\sigma}$ is the Cauchy stress tensor, $\dot{\boldsymbol{\varepsilon}}_{\boldsymbol{vp}}$ is the viscoplastic strain rate tensor, and ρ is the density of the material.

The rate of temperature increase is calculated from:

$$\dot{\Theta} = \frac{\chi \dot{\mathcal{D}}_p}{c} \tag{9}$$

where χ is the proportion of the plastic dissipation energy converted to heat (Taylor and Quinney 1933); and c is the specific heat capacity of the material.

In this study, the density ρ of the steel is assumed to be 7850 kg m^{-3}; χ is assumed to be 0.9, as proposed by Meyers (1994); and Θ_m, Θ_r, m_x and c are assumed to be 1527 °C, 20 °C, 1.071 and 452 J kg^{-1}°C^{-1}, respectively, as given by Dey et al. (2004) for Weldox 700 E steel, which is graded as S690QL (CEN 2019). The quasi-static tension and SENB simulations are assumed to be isothermal, with X (Eq. 7) always equal to one.

2.4 Damage

The damage-softening coefficient β is described by the model of Li and Wierzbicki (2010), as given in Eq. (10):

$$\beta = \begin{cases} 1 & D \leq 1 \\ \left(\dfrac{D_c - D}{D_c - 1}\right)^m & 1 < D < D_c \\ 0 & D = D_c \end{cases} \tag{10}$$

where D is the damage indicator; D_c is the critical damage at which the strength is fully degraded to 0; and m is the damage softening exponent.

In this study, linearity is assumed for the softening behaviour with respect to D, such that $m = 1$. A D_c of 1.3 is assumed, based on calibrations of the present model to S690QL and AH36 steel by Wong and Walters (2025) together with the observation that similar types of steels from different studies have similar D_c: 2.1–2.3 for low-alloy steel pipes (Sakonder et al. 2022), 1.2–1.4 for nickel-chromium Inconel alloy (Sarzosa et al. 2022; Algarni et al. 2015) and 1.2–1.3 for hot-rolled low carbon structural steel (Wong and Walters 2025; Chen et al. 2023).

The damage D builds up according to the accumulation of incremental equivalent plastic strains relative to the stress-state-dependent instantaneous damage initiation strain ε_f, as described by Eqs. (11) and (12), the strain-based formulation of the modified Mohr-Coulomb (MMC) model (Bai and Wierzbicki 2010).

$$D = \int_0^{\varepsilon_p} \frac{1}{\varepsilon_f} \, d\varepsilon_p \tag{11}$$

$$\varepsilon_f = \left\{ \frac{K}{c_2} \left[c_3 + \frac{\sqrt{3}}{2 - \sqrt{3}} (1 - c_3) \left(\sec \frac{\bar{\theta}\pi}{6} - 1 \right) \right] \times \left[\sqrt{\frac{1 + {c_1}^2}{3}} \cos \frac{\bar{\theta}\pi}{6} + c_1 \left(\eta + \frac{1}{3} \sin \frac{\bar{\theta}\pi}{6} \right) \right] \right\}^{-\frac{1}{n}} \tag{12}$$

where η is the stress triaxiality; $\bar{\theta}$ is the normalised Lode angle; and c_1, c_2 and c_3 are the MMC model parameters.

For the ease of calibration and for obtaining a physical sense of the effect of changes in the paramaters, the MMC parameters are normalised and expressed as C_1, C_2 and C_3, in the units of strains, as shown in Eqs. (13) to (16):

$$C_1 = \left(\frac{c_2}{c_3 K Z} \right)^{\frac{1}{n}} \tag{13}$$

$$C_2 = \left(\frac{2c_2}{K} \right)^{\frac{1}{n}} \tag{14}$$

$$C_3 = \left(\frac{\sqrt{3} c_2}{K c_3} \right)^{\frac{1}{n}} \tag{15}$$

where Z is given by:

$$Z = \sqrt{\frac{1 + {c_1}^2}{3}} + 2.5 c_1 \tag{16}$$

In the triaxiality-independent instance ($c_1 = 0$) of the MMC strain locus, C_1 and C_3 are both equal to the minimum strain in the locus, occurring at $\bar{\theta} = 0$, and C_2 is equal to the maximum strain in the locus, occurring at $\bar{\theta} = \pm 1$. Furthermore, C_1 is always equal

to the value of the fracture strain for ($\eta = 2.5, \bar{\theta} = 0$), the perfectly plastic, plane-strain solution for the stress state at a crack tip, and the smaller C_1 is than C_3, the greater the triaxiality dependence.

A cut-off for the negative-triaxiality damage initiation strains is implemented numerically at $\eta = -1/3$ (Bao and Wierzbicki 2005) by additionally increasing the damage initiation strain ε_f gradually towards infinity as η drops below $-1/3$. For the purpose of numerical convergence in the solution of the yield function (Eq. (1)), the ε_f for $\eta \geq 3.5$ is kept constant at its value when $\eta = 3.5$. Such values of η typically only occur when the element is already highly damaged and degraded, so this approximation is not expected to change the solution.

Using experiments on an AH36 and an S690 steel, Wong and Walters (2025) have shown that the assumption of triaxiality independence, together with the aforementioned understanding of the correlation of D_c to the steel type and the assumption of linear degradation ($m = 1$), performs well in reducing the number of damage calibration parameters for weakly-triaxiality-dependent steels to only two (C_2 and C_3) while simulating the responses of the tensile, Charpy and SENB tests well. This is effectively a capitalisation on the weak triaxiality dependence of the steels in the medium-to-high triaxiality range, which is the range experienced in the tensile test as it necks and in the crack planes of the Charpy and SENB tests. This quality of Lode-angle dependence with triaxiality independence has also been noted in Xue's (2009; 2010) modelling of Clausing's (1970) experiments on several structural steels and of experiments on aluminium alloy by Banabic et al. (2005). Additionally, this effect is further compounded by the observation (Wong and Walters 2025) that, due to crack tip blunting effects, the average triaxialities η calculated over $0 \leq D \leq 1$ experienced in key crack-front elements in the two tests as the damage D progresses are closer together, between around 1.1 and 1.3, than suggested by the difference in peak triaxialities ($\eta \sim 2.2$ in the SENB test and $\eta \sim 1.7$ in the Charpy test).

A damage locus that is described by two parameters can be calibrated using only two types of tests, given that they cover distinct stress states which are in the stress-state range of interest, and material certificates provide the results of two such tests in the form of A and C_v. Furthermore, it was observed that for key portions of the behaviour in the SENB and Charpy tests, namely well beyond the occurrence of the critical J_Q and up to 70% of the dissipation of C_v, the stress states in the Charpy and SENB are very similar, being determined by extensive tunnelling behaviour with little or no slant fracture. (In Section 4 below, it will be seen how the difference due to the later part of the C_v dissipation contributes to variations in the correlations between C_v and the J_Q initiation toughness.) Due to the similar tunnelling behaviour in a significant portion of the tests, a calibration based on the Charpy tests provides a similar range of stress states as is provided by the calibration to a SENB test (Wong and Walters 2025). In light of this, this study adopts the above assumptions for the present database of S690 steels in order to calibrate the material models for a large number of these steels, namely calibrating C_2 and C_3 based on the available A and C_v. The calibrated materials are then used to simulate the SENB test in order to construct numerically, mechanistically founded correlations between C_v and J_Q which take into account the other properties, such as σ_y/σ_u and A.

It is worth mentioning that, despite the effectiveness of the assumption of triaxiality independence for the purpose of the present work, this assumption is generally not suitable for describing axisymmetric tests (Wierzbicki et al. 2005) and tests on steels with strong triaxiality dependence in the range of triaxialities of interest. Notably, even metals with low pressure sensitivity in the medium to high triaxiality ranges are generally pressure-sensitive in the very-low-triaxiality range (Xue 2009).

3 Relationship between material certificate data and damage parameters

A parametric study varying the σ_y/σ_u and the key damage calibration parameters (C_2 and C_3) of the aforementioned material model in finite-element simulations of the Charpy (Fig. 2) and tensile (Fig. 3) test is performed in order to obtain sets of material certificate values with their corresponding damage parameters. For each (σ_y/σ_u, C_2, C_3) combination, both the Charpy and the tensile tests are simulated and then post-processed to obtain the A and C_v. This allows the subsequent deduction of the relationship between (C_2, C_3) and (A, C_v, σ_y/σ_u) using regression analysis of the numerical results.

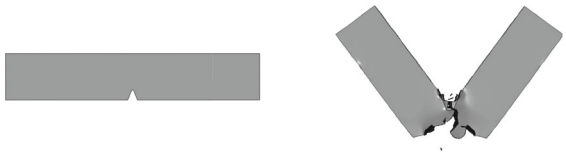

(a) Before loading. (b) After loading.

Fig. 2 Example Charpy simulation from the parametric study. ($\sigma_y/\sigma_u = 0.94$; $C_2 = C_3 = 0.7$)

A is here found using the definition of A_ε, the engineering strain when the force first drops below zero, which has been found (Wong and Walters 2025) to give a sufficiently close approximation of the value based on the standard A definition (ISO 2019) of summing the length of the broken gauge section and dividing the sum by the original gauge length, i.e. it is assumed that $A = A_\varepsilon$. The Charpy energy C_v is taken to be the total kinetic energy lost from the striker by the time the force has become stable around zero.

3.1 Parametric study

The simulations are performed in Abaqus Explicit 2022 (DS Simulia 2022) with the use of a user-defined material subroutine for the implementation of the material model. Eight-noded linear solid elements with reduced integration and hourglass control (C3D8R) are used. As a result of a mesh sensitivity study, elements with characteristic sizes l_c of 0.12 mm and 0.06 mm, respectively, were used in the fracture zones of the tensile and Charpy tests, where l_c is the cube root of the volume of an undeformed element. Mass scaling was applied to the Charpy and tensile test to decrease the computational time. In the simulations of the quasi-static tensile tests, the mass was increased by a factor of 1×10^9, and the kinetic energy was checked to be less than 1 % of the total internal energy, except for the beginning of the simulation when the load application boundary accelerates to the quasi-static testing velocity. In the simulations of the dynamic Charpy tests, the mass was increased by a factor of 25, a value which is seen to produce a negligible difference in C_v in a previous mass scaling factor sensitivity study (Wong and Walters 2024). The coefficient of friction between contact surfaces in the Charpy simulations was assumed to be 0.15.

Table 1 Range of σ_y and σ_y/σ_u considered

σ_y [MPa]	730	750	770	810	850
σ_y/σ_u [-]	0.92	0.93	0.94	0.96	0.97

3.1.1 Parametric space selection

Table 1 gives the σ_y and σ_y/σ_u values that are considered in the parametric study. Although variation in the σ_y/σ_u is seen for steels with the same grade and the same σ_y, a higher σ_y is generally accompanied by a higher σ_y/σ_u. Therefore, the σ_y/σ_u is here made to vary with the σ_y in order to reduce the size of the parametric space while reflecting the general trend. Including a numerical dataset with varying σ_y/σ_u for fixed σ_y would shed further light on the separate effects of σ_y/σ_u and σ_y, but is outside the scope of this already computationally expensive study. It is also worth noting that, because of the range of σ_y/σ_u considered and the use of Eqs. (4) and (5), ε_{sh} and ε_u are assumed to be constant in this study. For each σ_y/σ_u, a series of simulations are run, using all the combination pairs of C_2 and C_3 values that can be made from [0.4, 2.6, 5.1, 7.6] and [0.4, 0.7], respectively, with the exception that C_2 is set to equal C_3 in pairs where $C_2 < C_3$, since $C_2 < C_3$ does not align with experimental observations (see descriptions of Eqs. (14) and (15) above). Additionally, a reduced set of runs, considering a sparser set of σ_y/σ_u values, [0.92, 0.94, 0.97], is performed for the combination pairs of C_2 and C_3 values that can be made from [0.4, 2.6, 5.1, 7.6] and [0.5], to provide more numerical data while keep the computing costs within reasonable limits.

The values chosen for σ_y and σ_y/σ_u are based on the database of material certificates provided by Huisman BV, from which 77 steels are used to form a parametric space, by discretising the σ_y domain into intervals, and taking the σ_y/σ_u predicted by a least-squares fit to these 77 steels, as shown in Fig. 4 and Eq. (17):

$$\frac{\sigma_y}{\sigma_u} = \frac{1}{1 + \left(\frac{482}{\sigma_y}\right)^6} \tag{17}$$

where σ_y and σ_u are expressed in megapascals.

The dataset of 77 steels is a result of the following filtering criteria applied to the database. First, only steels with the equivalent grades of StE690 and S690Q (CEN 2019), which have the same minimum tough-

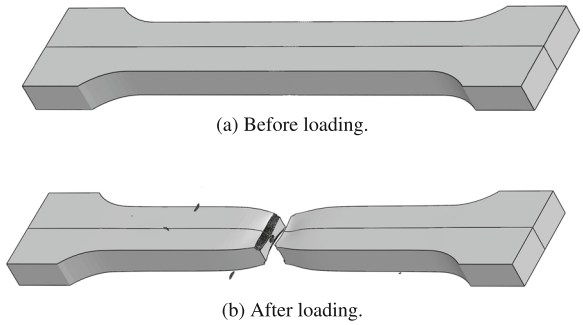

(a) Before loading.

(b) After loading.

Fig. 3 Example tensile simulation from the parametric study, with plane of symmetry. ($\sigma_y/\sigma_u = 0.94$; $C_2 = C_3 = 0.7$)

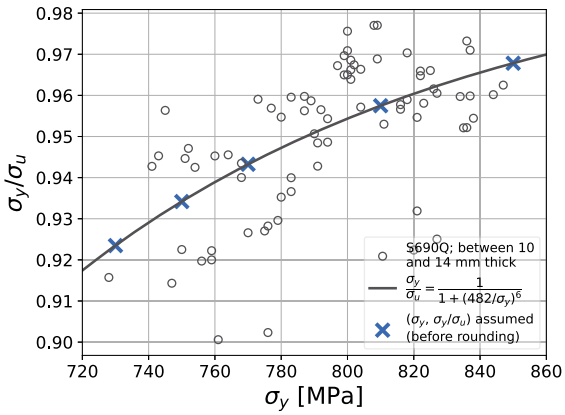

Fig. 4 σ_y/σ_u and σ_y assumed in the parametric study, based on fit to database

ness standard, are included in the dataset. Second, only steels with a thickness between 10 and 14 mm were included in the dataset. In the tensile test simulations, the steel is assumed to be 12 mm and modelled with a standard (IACS 2023) 25 mm width and proportional gauge length. The relatively small range of thicknesses in the dataset, centred around the value assumed in the simulations, is used so that more materials are included in the dataset while limiting any potential thickness effects that might exist despite the proportionality of the specimens (ASTM 2024). Finally, only steels for which all the three C_v repetitions reported on the material certificate were larger than 100 J, and for which all three repetitions did not differ from each other by more than 50 J, were included in the dataset. This is to ensure that the Charpy tests considered in the dataset involved fully ductile behaviour even though these tests performed at −20 °C according to the corresponding material standard (CEN 2019), since the simulations do not account for any transition to unstable cleavage fracture.

3.1.2 Charpy testing temperature assumed in the parametric study

The tensile tests, which are used to deduce the parameters describing the plastic strain-hardening behaviour assumed in the Charpy and tensile simulations, were performed at ambient temperature, while the Charpy tests were performed at −20 °C. The temperature affects the plastic flow stress of materials, but this temperature difference of −40 °C could be expected to make a relatively small difference in the flow stress (Yan et al. 2014). To ascertain the significance of this difference, Charpy simulations accounting for temperatures of −20 °C and −60 °C were additionally performed for the calibrated S690QL steel investigated in Wong and Walters (2025), which was one of the materials for which detailed experimental comparisons were carried out as part of the validation of the present material modelling approach. Since the Johnson-Cook-based model described above (Eq. 7) is suitable only for thermal softening at temperatures above room temperature, the effect of the lower temperature is included here by directly modifying the entire plastic strain-hardening curve according to the BS 7910 (BSI 2019) equation recommended for assessment temperatures below room temperature and above −196 °C, given the room temperature yield strength:

$$\sigma_{y,cold} = \sigma_{y,room} + \frac{10^5}{491 + 1.8\Theta} - 189 \tag{18}$$

where $\sigma_{y,cold}$ [MPa] is the estimated flow stress at low temperature, $\sigma_{y,room}$ [MPa] is the flow stress at room temperature, and Θ [°C] is the temperature.

For simplicity, this relationship is assumed to be applicable directly to the true plastic strain hardening stress $\bar{\sigma}$ (Eq. (2)), by setting $\bar{\sigma} = \sigma_{y,room}$, such that the temperatures of −20 °C and −60 °C result in a uniform increase to the $\bar{\sigma}$ of 31 MPa and 72 MPa, respectively,

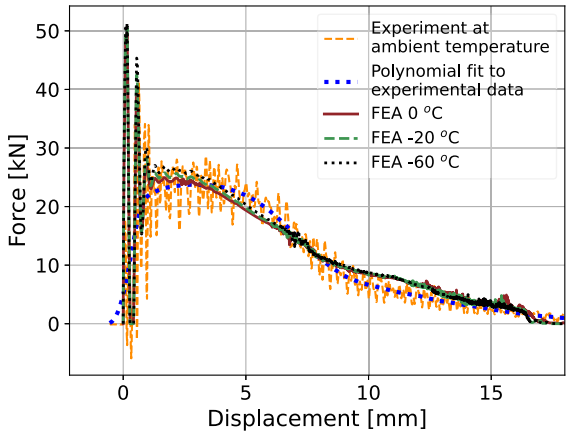

Fig. 5 Charpy simulations of S690QL steel at −60 °C, −20 °C and 20 °C

for all ε_p. This assumption of uniform increase is in line with the observed effect of lower temperatures on the shape of the stress-strain curves as seen in Yan et al. (2014). The other material parameters, including the thermal softening parameters, are kept the same (Table 2), and the simulations start at room temperature with the uniformly increased plastic strain-hardening curve due to the lower temperature, such that the thermal softening model (Eq. 7) is assumed to act based on the temperature difference relative to the starting temperature.

The simulation results (Fig. 5 and Table 3) indicate that a testing temperature of −20 °C, and the associated 31 MPa increase in flow stress relative to room temperature conditions, makes a negligible difference to both the Charpy force-displacement curve and the Charpy energy, assuming that the Charpy test behaviour is in the fully ductile regime. In contrast, the temperature rise around the notch due to adiabatic effects, which could be as much as 350 °C (Tanguy et al. 2005), would lead to a 20 % decrease in the flow stress, given the present thermal softening parameters (Table 2). Therefore, the Charpy simulations in the parametric study, which do take the thermal softening effects into account, are performed assuming room temperature plastic strain-hardening properties, although the Charpy tests were performed at −20 °C.

3.1.3 Significance of the yield-to-tensile strength ratio σ_y/σ_u

Classically, the σ_y/σ_u is related to the amount of strain hardening through the application of the Considère (1885) uniaxial necking criterion to a Hollomon (1945) power curve (Eq. (19)) that passes through the yield point in the true stress versus true total strains plot, which results in Eqs. (20) and (21) (Zhu and Leis 2005):

$$\bar{\sigma} = K_H {\varepsilon_t}^{n_H} \tag{19}$$

$$n_H = \varepsilon_{u,t} \tag{20}$$

$$\frac{\sigma_y}{\sigma_u} = \frac{1}{1+\varepsilon_y}\left(\frac{e\ln(1+\varepsilon_y)}{n_H}\right)^{n_H} \tag{21}$$

where $\bar{\sigma}$ is the true stress, K_H is the Hollomon strength coefficient, n_H is the Hollomon hardening exponent, ε_y is the engineering yield strain, e is the Euler's number, ε_t is the true total strain, and $\varepsilon_{u,t}$ is the true total strain corresponding to the occurrence of necking instability.

This enables the theoretical hardening curve (i.e. strength coefficient K_H, hardening exponent n_H, and hence its slope) up to the point of necking for Hollomon-type materials to be found, given only σ_y/σ_u, σ_y and E, thereby relating σ_y/σ_u, a ratio of stresses only, to the strain hardening slope. This forms the basis for the use of σ_y/σ_u as an indicator for the strain hardening behaviour in some design rules concerning failure modes sensitive to the hardening slope, such as the plastic buckling of beams (Wong and Walters 2023; Studer and Taras 2023).

Although σ_y/σ_u could function adequately as an indirect indicator for strain hardening in specifying reference limits for specific design cases, the theoretically derived Hollomon-based relationship between the necking strain and σ_y/σ_u is not generally applicable, and a range of uniform elongation values is observed for a given σ_y/σ_u in typical structural steels (Yun and Gardner 2017), in violation of Eqs. (20) and (21). This can be attributed to the restrictions imposed on the shape of the strain hardening curve when assuming the Hollomon rule. Therefore, a more versatile plastic strain hardening rule (Eq. (2)), which consists of a yield plateau followed by a Swift curve, is adopted in the present study.

Due to the presence of the Swift offset parameter in Eq. (2), n alone is no longer sufficient to fully describe the hardening slope. To quantify the relationship between σ_y/σ_u and the amount of hardening for the present hardening rule, an expression for the average slope g in the true stress versus true plastic strain space, between the end of the yield plateau $\varepsilon_{sh,p}$ and the occurrence of necking instability $\varepsilon_{u,p}$, is derived:

Table 2 Calibrated material parameter values from Wong and Walters (2025) for an S690QL steel, used in combination with Eq. (18) for the low-temperature ductile simulations

		S690QL
(a) Plasticity and damage		
σ_y	[MPa]	836
$\varepsilon_{sh,p}$	[-]	0.0438
ε_0	[-]	0.0413
K	[MPa]	984.1
n	[-]	0.0192
C_1	[-]	0.47
C_2	[-]	8.50
C_3	[-]	0.47
m	[-]	1
D_c	[-]	1.3
(b) Rate dependence, thermal effects and elasticity.		
C	[s^{-1}]	40524.5
q	[-]	3.3
$\dot{\varepsilon}_{p,uni}$	[s^{-1}]	0.00025
$\dot{\varepsilon}_{p0}$	[s^{-1}]	0.00025
Θ_m	[°C]	1527
Θ_r	[°C]	20
m_x	[-]	1.071
c	[J kg^{-1}°C^{-1}]	452
E	[MPa]	206064
ν	[-]	0.3

Table 3 Charpy energy values in simulations with flow stress modified to account for lower temperatures

		Test	Simulations		
Θ	[°C]	~ 20	−60	−20	20
C_v	[J]	204.2	224.7	219.6	217.1

$$g = \frac{\int_{\varepsilon_{sh,p}}^{\varepsilon_{u,p}} \frac{\mathrm{d}\bar{\sigma}}{\mathrm{d}\varepsilon_p}\,\mathrm{d}\varepsilon_p}{\varepsilon_{u,p} - \varepsilon_{sh,p}} = \frac{\sigma_y(1+\varepsilon_{sh})}{(\varepsilon_{sh,p} - \varepsilon_{u,p} + n)^n(\varepsilon_{u,p} - \varepsilon_{sh,p})} \cdot (n^n - (\varepsilon_{sh,p} - \varepsilon_{u,p} + n)^n) \tag{22}$$

where n is related to σ_y/σ_u by:

$$\frac{\sigma_y}{\sigma_u} = \frac{(1+\varepsilon_u)(\varepsilon_{sh,p} - \varepsilon_{u,p} + n)^n}{n^n(1+\varepsilon_{sh,p})} \tag{23}$$

Eqs. (22) and (23) show that the average strain hardening slope becomes dependent on ε_{sh} and ε_u, in addition to n, σ_y, σ_u and E. On the other hand, the average slope g_H for the Hollomon case depends only on n_H, σ_y, σ_u and E, as given by Eq. (24):

$$g_H = \frac{\int_{\varepsilon_{y,t}}^{\varepsilon_{u,t}} \frac{\mathrm{d}\bar{\sigma}}{\mathrm{d}\varepsilon_t}\,\mathrm{d}\varepsilon_t}{\varepsilon_{u,t} - \varepsilon_{y,t}} = \frac{\sigma_u e^{n_H}(n_H{}^{n_H} - \varepsilon_{y,t})}{n_H{}^{n_H}(n_H - \varepsilon_{y,t})} \tag{24}$$

where $\varepsilon_{y,t}$ is the true total strain at the initial yield point, and e is Euler's number.

To illustrate the implication of this difference between g and g_H, the empirically obtained predictions for ε_{sh} (Eq. (4)) and ε_u (Eq. (5)) from Yun and Gardner (2017) are used to calculate g, which is then plotted together

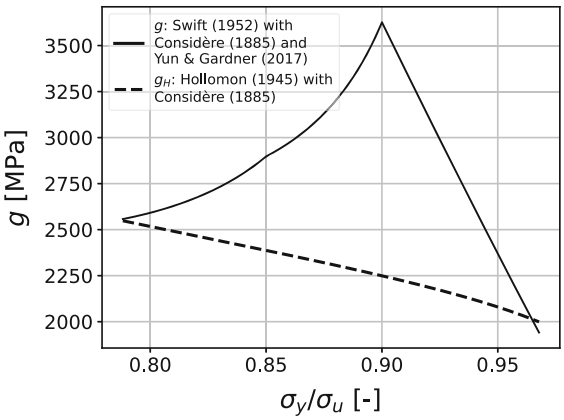

Fig. 6 Average hardening slope g against σ_y/σ_u

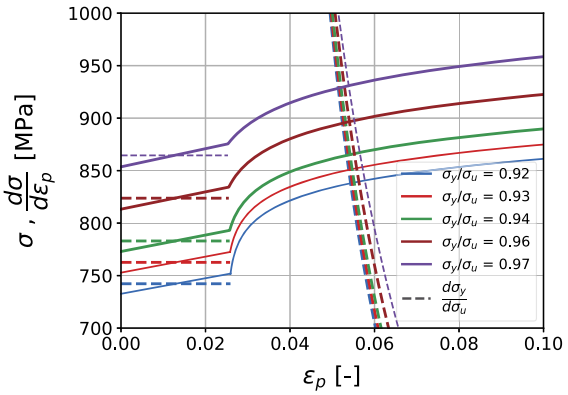

Fig. 7 Effect of varying σ_y/σ_u on the plastic strain hardening curve

with g_H, as shown in Fig. 6. The correlation between σ_y/σ_u and σ_y given in Eq. 17 is also assumed. Due to the dependence of g on ε_{sh} and ε_u, the relationship between the strain hardening slope g and σ_y/σ_u is not monotonic, in contrast with g_H. In the present study, the range of σ_y/σ_u is limited to $0.92 \leq \sigma_y/\sigma_u \leq 0.97$, which corresponds to values observed in the reference database of material certificates of S690 steels (discussed in Section 3.1.1). In this regime, ε_{sh} and ε_u remain constant according to Eqs. (4) and (5), and an increasing σ_y/σ_u is associated with a decreasing hardening slope (Fig. 6), as is normally expected. This is confirmed by the plot (Fig. 7) of the present hardening rule (Section 2.1) together with the Considère necking point, which illustrates how the hardening curve changes in the present study: the strength increases, the average hardening slope decreases, and the yield plateau length and necking strain stays constant, as σ_y/σ_u is increased from 0.92 to 0.97. However, it is important to note the range for which this applies and the presence of scatter observed in ε_{sh} and ε_u values in practice.

3.2 Regression of A and C_v on C_2 and C_3

The results of the parametric runs, together with a fitted relationship based on least-squares regression, are plotted in Figs. 8 to 11. The proposed regression model is given in Eq. (25) and is a result of fitting different trial models based on the trends observed in the data and choosing the one that best reflect the trends.

$$\begin{cases} C_v(C_2, C_3, \frac{\sigma_y}{\sigma_u}) = P_1 P_2{}^{\left(\frac{\sigma_y}{\sigma_u}-1\right)} C_2{}^{P_3} \\ \quad + P_4 P_5{}^{\left(\frac{\sigma_y}{\sigma_u}-1\right)} \frac{\sigma_y}{\sigma_u} C_3{}^{P_6} \\ \quad + P_7 P_8{}^{\left(\frac{\sigma_y}{\sigma_u}-1\right)} C_2{}^{P_9} C_3{}^{P_{10}} \\ A(C_2, C_3) = Q_1 C_2{}^{Q_2} + Q_3 C_3{}^{Q_4} + Q_5 C_2{}^{Q_6} C_3{}^{Q_7} \end{cases} \tag{25}$$

where P_i and Q_i are the fitting parameters, as shown in Table 4.

The data points in Figs. 8b, 9b and 10b show that σ_y/σ_u has no appreciable effect on A. Because σ_y/σ_u is assumed to vary monotonically with σ_y, this also implies that σ_y has little effect on A. The tiny variations seen in A with respect to changes in σ_y/σ_u seen in these plots appear as scatter with no consistent trend. Hence, it is assumed that σ_y/σ_u has no effect on A in this regime and does not appear as a variable in the equation for A. From Figs. 8 and 9, both A and C_v appear to have a power-law relation with respect to C_2 and C_3, although this is relatively weak between A and C_3, especially when C_2 is high. Additionally, Fig. 10a suggests that C_v has an exponential dependence on σ_y/σ_u. The proposed nature of the dependencies between the individual variables are summarised in Table 5. These determine the form of constituent terms chosen in the Eq. 25, i.e. $P_i{}^{\left(\frac{\sigma_y}{\sigma_u}-1\right)}$ for exponential relations and $P_i C_i{}^{P_j}$ or $Q_i C_i{}^{Q_j}$ for power relations.

The data points in Figs. 8 to 10 also reveal information about the coupling between the plasticity parameter σ_y/σ_u and the damage parameters C_2 and C_3. It can be seen that changes in C_3 non-linearly affects the

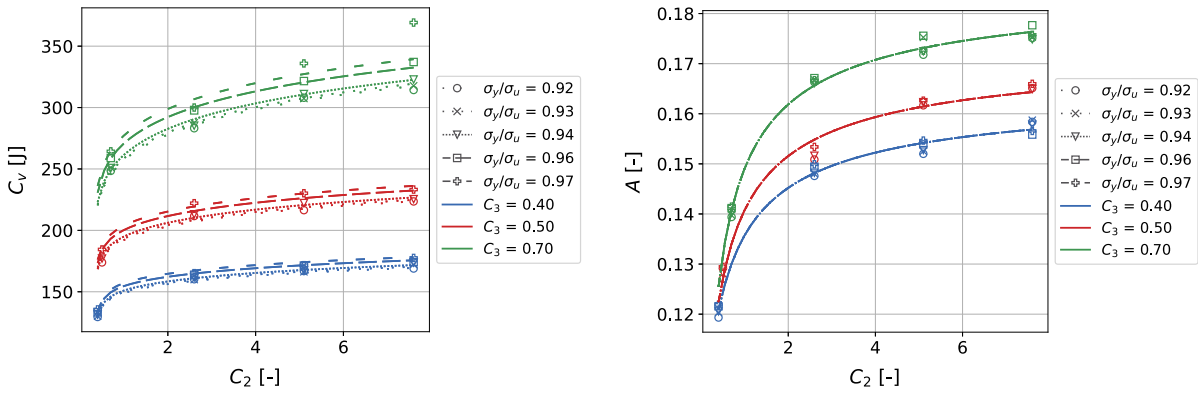

(a) C_v against C_2 (b) A against C_2

Fig. 8 C_v and A against C_2 from the parametric simulations

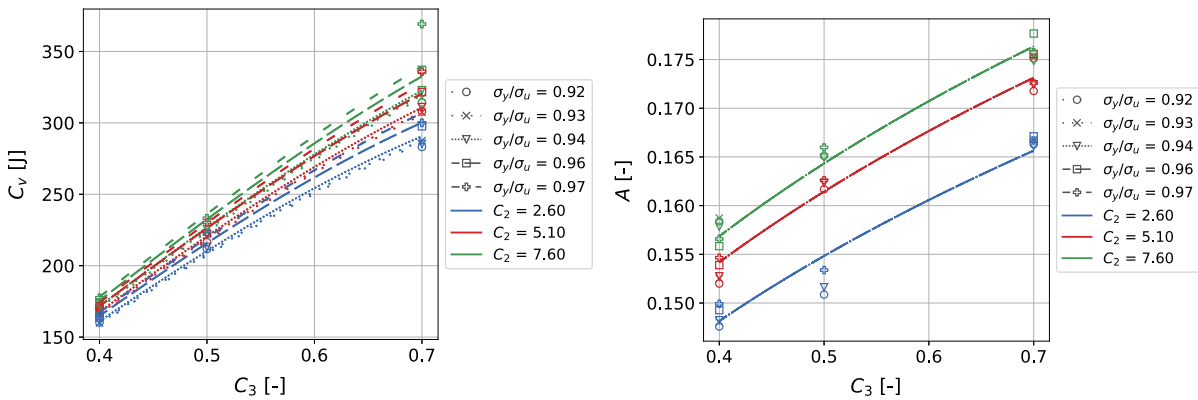

(a) C_v against C_3 (b) A against C_3

Fig. 9 C_v and A against C_3 from the parametric simulations

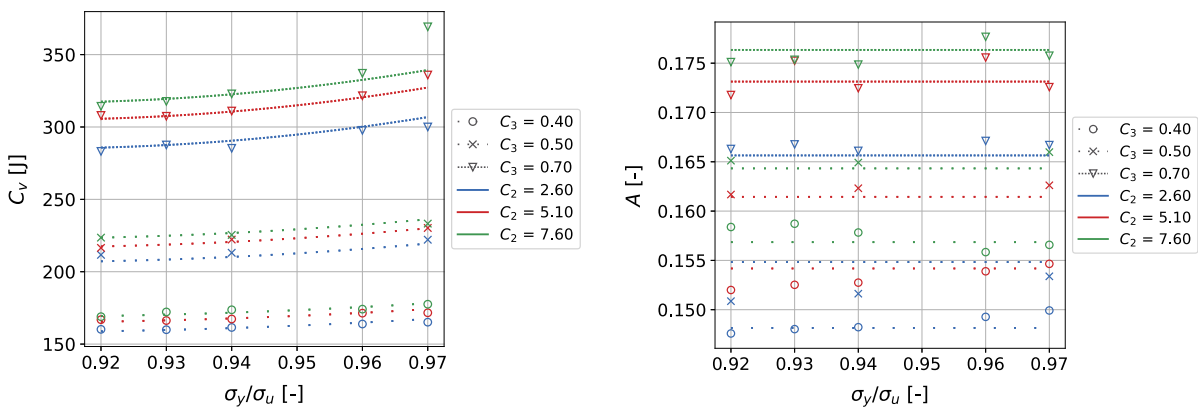

(a) C_v against σ_y/σ_u (b) A against σ_y/σ_u

Fig. 10 C_v and A against σ_y/σ_u from the parametric simulations

Table 4 Fitted calibration parameters

(a) P_i parameters

i	units	P_i
1	[J]	−0.89626
2	[-]	494.46
3	[-]	−3.2177
4	[J]	−22127
5	[-]	0.55185
6	[-]	2.0040
7	[J]	22481
8	[-]	1.6325
9	[-]	0.0027501
10	[-]	1.9707

(b) Q_i parameters

i	units	Q_i
1	[-]	5.0212
2	[-]	−0.84337
3	[-]	0.20165
4	[-]	0.21133
5	[-]	−5.0639
6	[-]	−0.84132
7	[-]	0.0026558

Table 5 Dependencies of C_v and A on C_2, C_3 and σ_y/σ_u

	C_2 [-]	C_3 [-]	σ_y/σ_u [-]
C_v [J]	Power	Power	Exponential
A [-]	Power	Power	None

way C_v is related to C_2 (Fig. 8a) and changes in C_2 non-linearly affects the way C_v is related to C_3 (Fig. 9a). The same can be said of the relationship between A, C_2 and C_3. Therefore, the terms $P_i {C_2}^{P_j} {C_3}^{P_k}$ and $Q_i {C_2}^{Q_j} {C_3}^{Q_k}$ are included in the equation for C_v and A, respectively. From Fig. 8a, 9a and 10a, the coupling effect is also seen to act between σ_y/σ_u, C_2 and C_3. So, multiplicative terms between $P_i {\left(\frac{\sigma_y}{\sigma_u}-1\right)}$, $P_i {C_2}^{P_j}$ and $P_i {C_3}^{P_j}$ are used in the equation for C_v.

Since C_2 and C_3 are normalised parameters representing, respectively, the maximum (at $\bar{\theta} = \pm 1$) and minimum (at $\bar{\theta} = 0$) strains in the triaxiality-independent strain-based MMC damage locus (see section on Damage above), some physical sense could be derived from these findings.

From Figs. 9 and 11, the effect of C_3 is stronger on C_v than on A. This could be related to how the tunneling effects in the Charpy test, which have been shown to have a dominant effect in the behaviour (Wong and Walters 2025), begin at mid-thickness in the specimen, where $\bar{\theta} = 0$. In contrast, $\bar{\theta}$ in the tensile test starts at 1 and gradually drops as necking occurs. The difference in the proportion of effects caused by C_2 and C_3 on C_v and A sheds light on the role played by each damage parameter in the process of calibration. While it is obvious that materials with high A and C_v are characterised by both high C_2 and high C_3, these results reveal infor-

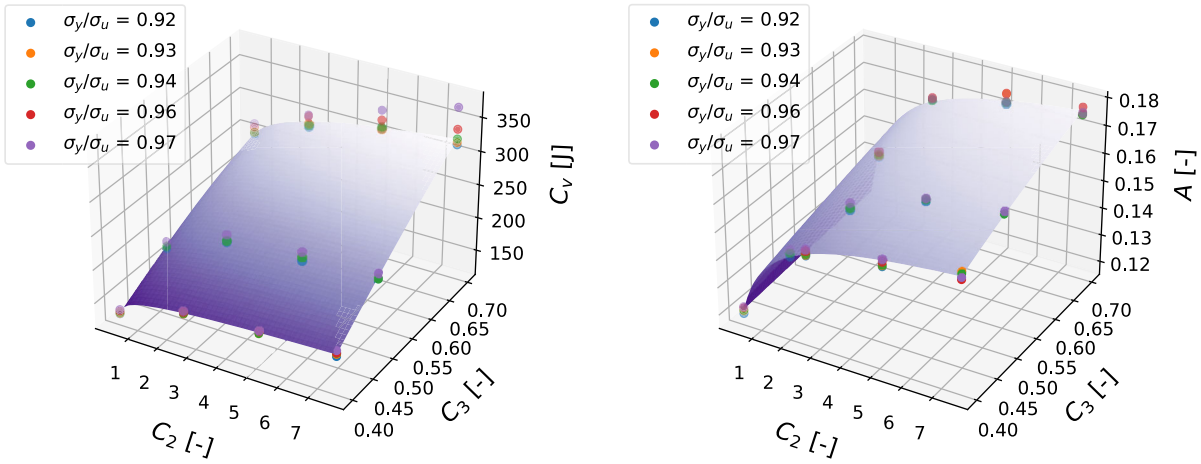

(a) C_v against C_2 and C_3

(b) A against C_2 and C_3

Fig. 11 C_v and A against C_2 and C_3 from the parametric simulations together with fitted surface (using $\sigma_y/\sigma_u = 0.94$ as an example)

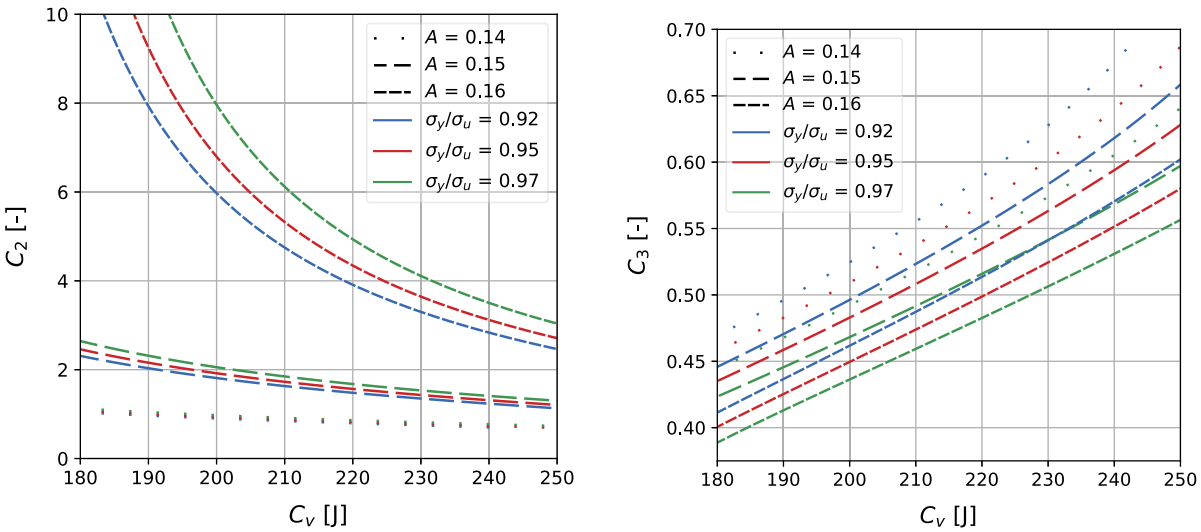

(a) C_2 against C_v

(b) C_3 against C_v

Fig. 12 C_2 and C_3 against C_v obtained from solving Eq. 25

mation about the trends that characterise materials with high notch toughness C_v but low uniaxial-test fracture elongation A. Fig. 11 suggests that for a material with triaxiality-independent damage behaviour, the combination of high C_v and low A is characterised by combinations of high damage initiation strains at $\bar{\theta} = 0$ and low damage initiation strains at $\bar{\theta} = 1$. Conversely, a combination of low notch toughness and high uniaxial-test fracture elongation is characterised by low C_2 and high C_3.

It is also worth noting that the effect of C_2 (the maximum strain of the damage initiation locus) on C_v, which was identified as being very weak in previous work by the present authors (Wong and Walters 2024), could in fact become significant if the variations in C_2 become very large (Fig. 8a).

Finally, given a set of material certificate values for a steel within the range of the parametric study, Eq. (25) can be solved numerically to find an estimation of the calibrated damage parameters C_2 and C_3. Natu-

rally, the range of A and C_v for which solutions exists has its bounds, as can be guessed from the surfaces shown in Fig. 11. Furthermore, the solution should not involve extrapolation beyond the range investigated by the parametric study. Fig. 12 shows the solutions of Eq. 25 for different C_v, σ_y/σ_u and A within the investigated range. It reveals that A has a stronger effect on the correlation between C_2 and C_v and the correlation between C_3 and C_v than does σ_y/σ_u, even when the coupling between plasticity and damage has been accounted for. To evaluate the consequences of this trend, observed in the internal damage parameters, for measured fracture properties, Eq. (25) is used in the next section to estimate the damage parameters and simulate the SENB fracture toughness test to obtain critical ductile fracture J-integral values, J_Q, for given combinations of A, C_v and σ_y/σ_u.

4 Correlation between C_v and J_Q

A total of 15 simulations of the SENB test (Fig. 13) were performed, for A varying between 0.14 and 0.16, σ_y/σ_u varying between 0.92 and 0.97, and C_v varying between 150 J and 250 J, as shown in Table 6. The results are plotted in Fig. 14, along with the upper-shelf J_Q - C_v conversion developed by Wallin (2001), which has been adopted in BS7910 (BSI 2019), and a similar correlation developed by Schindler (2001). Comparison to other similar upper-self correlations (Gioielli et al. 2000; Merkle and Johnson 1985; Eason and Nelson 1989; Eason et al. 1991; Kussmaul and Roos 1985; Sreenivasan 2014) is omitted due to differences in testing conditions and fracture toughness definitions used to obtain those correlations. A review on differences between the other proposed correlations can be found in Wallin (2001, 2021).

The Wallin (2001) correlation is obtained by solving Eqs. (26) to (29):

$$J_{1\,\mathrm{mm},W} = 0.53{C_v}^{1.28} \tag{26}$$

$$m_W = 0.133{C_v}^{0.256} - \frac{\sigma_y}{4664} + 0.03 \tag{27}$$

$$\sigma_{fW} \approx \sigma_y \left(1 + \frac{150}{\sigma_y}\right) \tag{28}$$

$$\frac{J_{QW}}{2\sigma_{fW}} + 0.2 = \left(\frac{J_{QW}}{J_{1\,\mathrm{mm},W}}\right)^{\frac{1}{m_W}} \tag{29}$$

where $J_{1\mathrm{mm},W}$ [kJ m^{-2}] is Wallin's J-integral at 1 mm crack extension; C_v [J] is the Charpy impact energy,

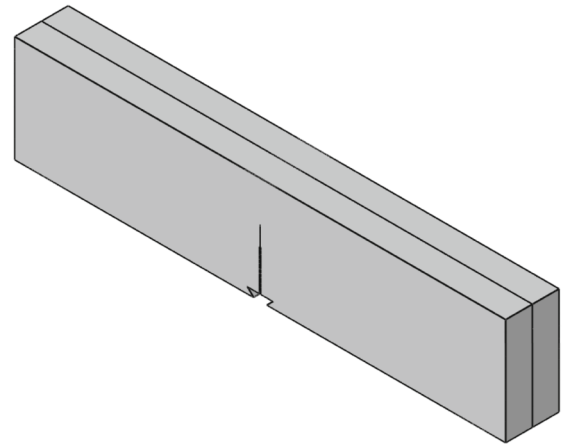

(a) Before loading.

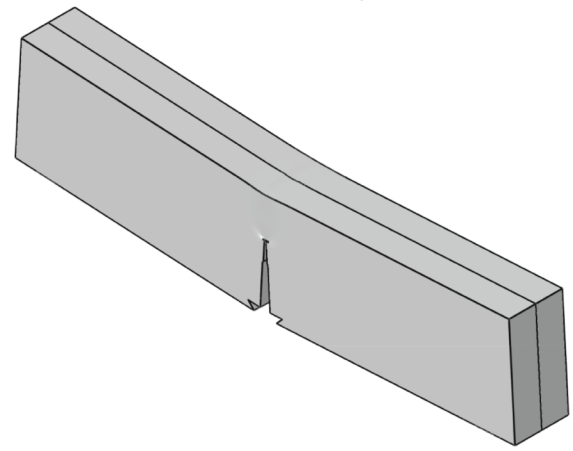

(b) After loading.

Fig. 13 Example SENB simulation from the parametric study (corresponding to $\sigma_y/\sigma_u = 0.95$; $C_v = 200$ J; $A = 0.15$), with plane of symmetry

m_W [-] is the Wallin J-Δa curve exponent, σ_y [MPa] is the yield strength, σ_{fW} [MPa] is the average flow stress according to Wallin (1995); and J_{QW} [kJ m^{-2}] is the critical J based on the 0.2 mm crack extension offset using the Wallin (2001) conversion from Charpy energy.

The Schindler (2001) correlation is obtained by solving Eqs. (30) to (33):

$$J_{1\,\mathrm{mm},S} = \frac{0.0250}{8^{m_S}}\left(1000C_v - 7.97U_f\right) \left(\varepsilon_u - \frac{\sigma_u}{E}\right)^{1-m_S} \tag{30}$$

$$m_S = \frac{3}{4}\left(1 + \varepsilon_u - \frac{\sigma_u}{E}\right)^{-1} \tag{31}$$

Table 6 Values of σ_y/σ_u for different combinations of A and C_v used for generating the simulations in the parametric study on fracture toughness from SENB testing

C_v [J] / A [-]	150	180	190	200	210	220	250
0.14	0.97	0.97	-	-	0.97	-	-
0.15	0.92, 0.95, 0.97	-	-	0.92, 0.95, 0.97	-	-	0.92, 0.95, 0.97
0.16	-	-	0.97	-	-	0.97	0.97

$$\sigma_{fS} = \frac{\sigma_y + \sigma_u}{2} \tag{32}$$

$$\frac{J_{QS}}{2\sigma_{fS}} + 0.2 = \left(\frac{J_{QS}}{J_{1\,\mathrm{mm},S}}\right)^{\frac{1}{m_S}} \tag{33}$$

where $J_{1\,\mathrm{mm},S}$ [kJ m^{-2}] is Schindler's J-integral at 1 mm crack extension; m_S [-] is the Schindler J-Δa curve exponent; C_v [J] is the Charpy impact energy; U_f [N mm^{-2}] is the specific energy or strain energy density of the tensile test, here approximated by the area under the engineering stress-strain curve; ε_u [-] is the uniform elongation expressed as a fraction; σ_u is the ultimate tensile strength; σ_y [MPa] is the yield strength, σ_{fS} [MPa] is the average flow stress according to Schindler (2001); and J_{QS} [kJ m^{-2}] is the critical J based on the 0.2 mm crack extension offset using the Schindler (2001) conversion from Charpy energy.

4.1 Implications of changes in A

Figure 14a shows how the correlation between J_Q and C_v varies for different A, when the σ_y/σ_u and σ_y are fixed. The parametric study shows that a higher J_Q is correlated with a lower A for a given C_v in this case. The Wallin (2001) correlation does not include A, but the Schindler (2001) correlation does show the same trend with A seen the parametric study, although its effect is so small it appears negligible. The A enters the correlation indirectly through U_f in Eq. (30), the specific energy of then tensile test, that is strongly correlated to A when the other engineering tensile test properties and, by extension, the plastic strain hardening properties are kept constant. From Eqs. (30) and (33), it can be seen that a decrease in U_f caused by a decrease in A leads to a increase in J_{QS} when all else is kept constant, even though this difference is so small that it is not visible in the plot (Fig. 14a).

Although both the present numerical results and Schindler (2001) indicate a weak negative correlation between A and J_Q, many sources report a positive correlation between some measure of ductile fracture initiation toughness (such as equivalent critical plane strain fracture toughness K_{IC}) and either the tensile test strain energy density (associated with the area under the stress-strain curve) or the tensile test fracture elongation, for various ductile metals including steels (Li et al. 2022; Shashank Dutt et al. 2025; Alexopoulos and Tiryakioglu 2009; Hirth and Froes 1977). Taking into consideration the mechanisms assumed in Schindler's model, in which ε_u accounts for strain hardening and U_f is used based on empirical grounds to account for the difference in the energies associated with cracked and uncracked geometries, an increase in A and U_f with the other engineering test properties kept constant can be considered to be associated with an increase in the portion of the energy dissipation associated only with the initial deterioration of the uncracked notch in the Charpy test, which is not reflected in J_Q values obtained from fracture toughness testing of a the pre-cracked test, such that the remaining portion of the C_v, which is correlated to the J_Q, decreases, reflecting a decrease in J_Q. However, due to the empirical nature of this use of U_f to account for the effect of the Charpy notch and the difficulty in accounting for these energies separately, it is difficult to confirm the validity of this hypothesis using Schindler's model.

On the other hand, in the present numerical study, this trend of increasing A being accompanied by decreasing J_Q can be explained, for the assumed triaxiality-independent damage model, using mechanistic considerations relating to the fracture initiation strains and energetic considerations through partitioning of the Charpy impact energy. First, considering how all the energy attributed to ductile fracture initiation is

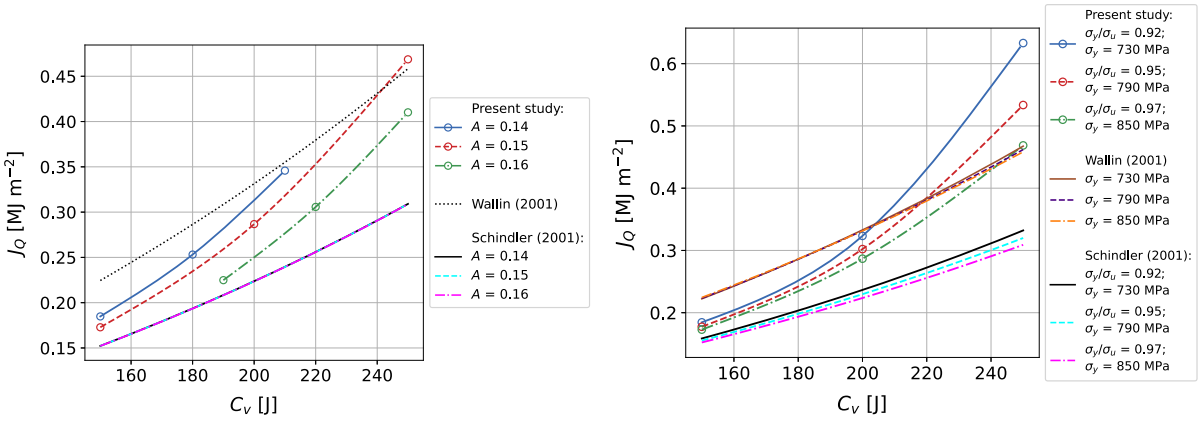

(a) J_Q against C_v for different A and fixed $\sigma_y/\sigma_u = 0.97$

(b) J_Q against C_v for different σ_y/σ_u and fixed $A = 0.15$

Fig. 14 J_Q against C_v; circles represent simulated data points

dissipated before the force peak in a ductile Charpy impact test (Fabry et al. 1993; Chaouadi and Fabry 2002) and how J_Q acts as a ductile fracture initiation measure evaluated close to the onset of stable crack extension in a fracture toughness test (ASTM 2023), J_Q is plotted in Fig. 15a against C_{vm}, the portion of the Charpy energy dissipated before the peak in the force-displacement plot from the instrumented Charpy test, instead of the total C_v. In this plot, variations due to A in the correlation between the Charpy measure and the J_Q measure dwindle. This reveals that differences in the C_v to J correlations observed for different A are related to differences in specifically the post-peak energy. This can in turn be related to the trend observed in the regression of A and C_v on C_2 and C_3 (Section 3).

The regression obtained in Section 3 (Fig. 12) indicates that maintaining a constant C_v while decreasing A involves decreasing C_2, the damage initiation strain at $\bar{\theta} = 1$, and increasing C_3, the damage initiation strain at $\bar{\theta} = 0$, in the assumed triaxiality-independent damage locus. A is strongly associated with $\bar{\theta} = 1$ because damage starts building up with $\bar{\theta} = 1$, the stress state induced by the pre-necking uniaxial testing conditions. ($\bar{\theta}$ gradually drops as the neck develops and damage accumulates.) The pre-peak C_{vm} is mainly influenced by C_3 because the initial cracking in a Charpy test starts with tunnelling at the mid-thickness of the specimen, which is characterised by a plane-strain state of $\bar{\theta} = 0$. The post-peak Charpy behaviour and hence the total C_v are, in contrast, also affected by C_2 in addition to C_3, because as the tunnelling progresses outward from mid-thickness towards the free surface and as shear lips develop, damage build-up involving the $\bar{\theta} = 1$ of the free surface occurs too. As for the fracture toughness test, cracking begins with tunnelling at the mid-thickness like the Charpy test, and the stable ductile crack initiation value J_Q corresponds to only a small amount of crack extension. J_Q is therefore much more strongly affected by C_3, just like the pre-peak C_{vm} from the Charpy test. The trends observed in the influence of A on the C_v to J_Q correlations (Fig. 14a) and the lack thereof in the C_{vm} to J_Q correlations (Fig. 15a) are therefore related to the prevailing stress states involved in the determination of each of the engineering properties. A lower A for constant C_v is associated with lower damage strains for $\bar{\theta} = 1$ and higher damage strains for $\bar{\theta} = 0$, which is tied to an increase in both the C_{vm} and the J_Q.

As a conceptual aid for the above discussion, a simplified qualitative summary of the strength of the interactions between the different variables is given in Table 7, and the evolution of the normalised Lode angle $\bar{\theta}$ at key locations in the tensile, Charpy and SENB simulations for the model calibrated to S690QL steel from Wong and Walters (2025) is shown in Fig. 16.

It is understood that the trend with which C_2 and C_3 changes for changing C_v or A, on which the preceding discussion is based, is limited by the assumption of triaxiality independence in the damage locus. If triaxiality dependence were included in the damage locus, the higher peak triaxialities in the SENB test

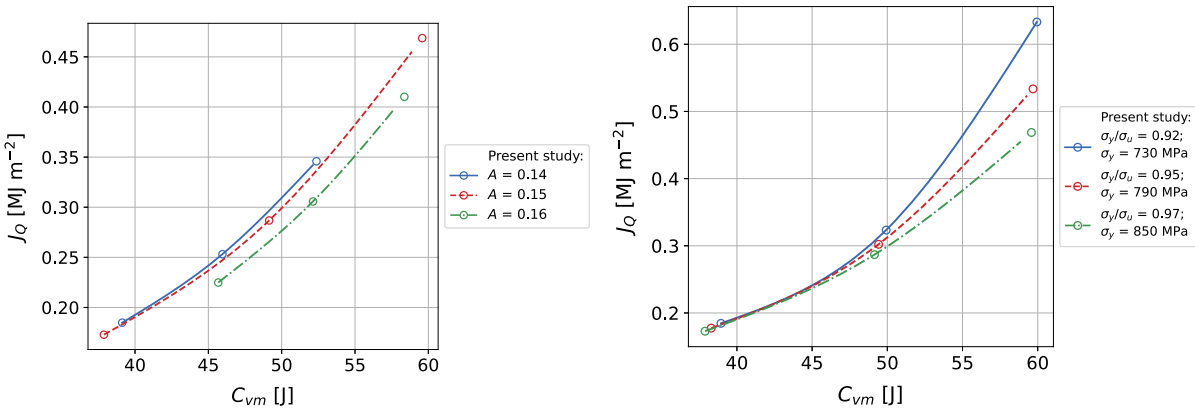

(a) J_Q against C_v for different A and fixed $\sigma_y/\sigma_u = 0.97$

(b) J_Q against C_{vm} for different σ_y/σ_u and fixed $A = 0.15$

Fig. 15 J_Q against C_{vm}; circles represent simulated data points

Table 7 Qualitative description of the strength of the interaction between the engineering parameters and material parameters as a conceptual aid

	C_{vm} [J]	C_v [J]	A [-]	J [MJ m^{-2}]
C_2 [-]	Weak	Strong	Strong	Weak
C_3 [-]	Strong	Strong	Weak	Strong
σ_y/σ_u [-]	Strong for high C_3; Weak for low C_3	Strong for high C_3; Weak for low C_3	None	Weak

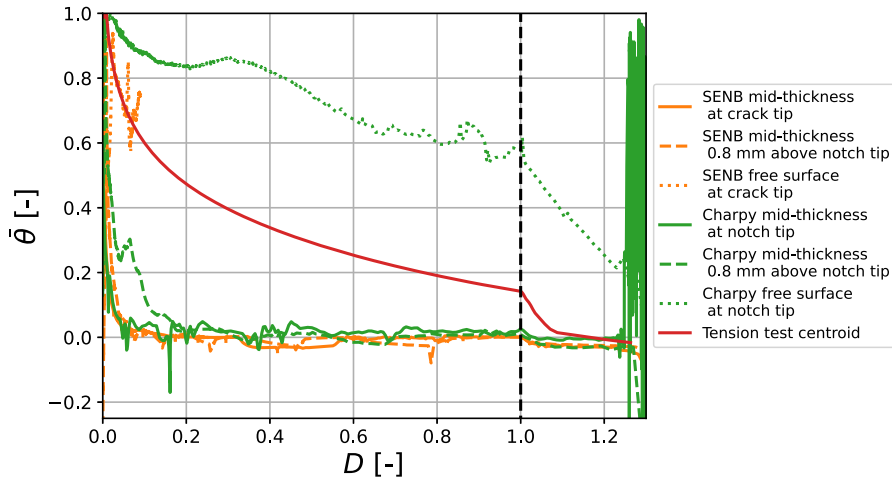

Fig. 16 Evolution of the normalised Lode angle $\bar{\theta}$ as damage D builds up at key locations in the tensile, Charpy and SENB simulations for a calibrated S690QL steel (from Wong and Walters (2025))

($\eta \sim 2.2; \bar{\theta} = 0$) compared to the Charpy test ($\eta \sim 1.7$; $\bar{\theta} = 0$) could be associated with lower damage initiation strains, giving combinations of damage parameters and simulations that result in a decreased J_Q and constant C_v for decreased A by virtue of decreased damage strains at high triaxiality ($\eta \sim 2.2; \bar{\theta} = 0$), despite the higher damage strains at peak Charpy triaxialities ($\eta \sim 1.7; \bar{\theta} = 0$) that would accompany the lower $\bar{\theta} = 1$ damage strains described above. This accounts for the discrepancy between the presently observed trend and that which is described in the literature (Li et al. 2022; Shashank Dutt et al. 2025; Alexopoulos and Tiryakioglu 2009; Hirth and Froes 1977) for A and J_Q. The presently observed negative correlation is one that is specific to the triaxiality-independent assumption. Nonetheless, the considerations relating to the

stress states and energy attributions behind these trends remain the same, and it remains that the correlation of J_Q with A is weak (Chatterjee (2020) correlation coefficient $\xi = -0.02$), and the J_Q is correlated to C_{vm} so strongly in comparison ($\xi = 0.79$) that changes in A have only a very weak effect on the J_Q–to–C_{vm} correlation.

4.2 Implications of changes in σ_y/σ_u

Fig. 14b shows how the correlation between J_Q and C_v varies for increasing σ_y/σ_u, with a correspondingly increasing σ_y (Eq. (17)), when the A is fixed. The Wallin (2001) correlation does not account for σ_y/σ_u, but predicts a higher J_Q for a lower σ_y, when all else is constant. The parametric study suggests that this trend still holds when the σ_y is accompanied by a higher σ_y/σ_u, with the difference that a slightly larger effect on the J_Q is predicted when the C_v is large. The effect of the increasing σ_y/σ_u and σ_y on J_Q observed here also agrees with the trend seen in the Schindler (2001) correlation. Nonetheless, the change in J_Q due to changing σ_y/σ_u and σ_y is small in comparison to that due to the change in C_v. At a C_v of 200 J, a change in σ_y/σ_u from 0.92 to 0.97, a range which spans 60% of the σ_y/σ_u range of the considered dataset (Fig. 4; Section 3.1.1), and includes 80% of the number of observations in the dataset, leads to only a 15% change in J_Q. The same change is effected by a change in C_v corresponding to a mere 5% of the range spanned by the C_v values in the considered dataset.

Comparing Figs. 14b and 15b, it is worth noting that although varying σ_y/σ_u has a smaller effect on the correlation between J_Q and C_{vm} than on the correlation between J_Q and C_v for low C_{vm} and low C_v, this does not apply to high C_{vm}. This is unlike the effect of variations in A on the C_{vm}–to–J_Q correlation, where the effect of the variation in A is seen to be small for all C_{vm}. Nonetheless, considering C_{vm} instead of C_v still has the effect of reducing the influence of variations in σ_y/σ_u on the prediction of fracture toughness from the Charpy data.

5 Conclusions

A numerical investigation of the correlation between J_Q and C_v and how it is affected by variations in A, σ_y/σ_u and σ_y has been performed using a rate- and temperature- dependent damage-softening plasticity model. To this end, a parametric study, involving a range spanned by a set of material certificate data and some empirical assumptions deduced from the dataset, was carried out, in which the SENB fracture toughness test was modelled for varying A and C_v, assuming correspondingly varying damage parameters which are calibrated based on the C_v and the A. The calibration was obtained from a regression analysis of C_v and A on material parameters C_2, C_3 and σ_y/σ_u, performed on a series of Charpy and tensile simulations for each of 52 combinations of C_2, C_3 and σ_y/σ_u values spanning the parametric space. The following conclusions are drawn from this study.

The pre-peak energy from the force-displacement plot in an instrumented ductile Charpy test C_{vm} has a stronger ($\xi = 0.79$) and more independent correlation with J_Q than does C_v ($\xi = 0.57$; Figs. 14 and 15). J_Q is predominantly related to the onset of ductile crack extension, but C_v includes a significant amount of energy attributed to continued ductile crack propagation. On the other hand, C_{vm} includes less of this crack propagation energy but includes all the energy up to the onset of ductile fracture and is thus more closely tied to J_Q. Developing and making use of correlations between C_{vm} and J_Q would result in more consistent predictions of ductile fracture initiation toughness than given by correlations between C_v and J_Q.

The σ_y/σ_u ratio has a weak correlation with C_{vm} ($\xi = 0.17$) and with J_Q ($\xi = 0.17$), especially for low-value ranges of C_{vm} and J_Q. The correlation between C_{vm} and J_Q themselves is far stronger ($\xi = 0.79$), such that changes in C_{vm} can be seen to give predictions of far more significant changes in J_Q than changes in σ_y/σ_u could be related to (Fig. 15b). The σ_y/σ_u ratio alone, without the information C_{vm} or C_v, is not useful for ductile fracture initiation toughness prediction.

For a model with a triaxiality-independent, Lode-dependent strain-based damage locus, the A is weakly and negatively correlated to J_Q for a constant C_v. Changes in A appear to affect the correlation between C_v and J_Q because A is correlated to the later-stage portion of the C_v energy, broadly associated with $\bar{\theta} = 1$, corresponding to both the uniaxial tensile pre-necking stress state and the free-surface stress state which becomes relevant with significant ductile crack propagation in the Charpy specimen. For a constant C_v, a decrease in A is correlated with a decrease in

that later-stage proportion of the energy, such that the C_{vm} and J_Q associated with fracture initiation increase. Even though the negative trend of the correlation between C_v and J_Q seen in the numerical results due to the assumption of triaxiality independence does not agree with experimental observations (Li et al. 2022; Shashank Dutt et al. 2025; Alexopoulos and Tiryakioglu 2009; Hirth and Froes 1977), it remains that J_Q is much more strongly correlated to C_{vm} than to A. Differences in A only have a small effect on the correlation (Fig. 15a) between J_Q and C_{vm}, which acts as a more reliable indicator than C_v. Due to this, the A alone, without C_{vm} or C_v, is in general not useful for ductile fracture resistance considerations.

Although varying σ_y/σ_u and A has some effect on how the total notch energy C_v is correlated to J_Q, it does not reflect a significant effect on the ductile fracture initiation toughness but is rather associated with the fact that the C_v includes a significant portion of energy for stable ductile propagation and fracture occurring at the specimen's free surface, while J_Q primarily concerns the onset stage of stable ductile tunnelling behaviour at the centre of the specimen. The σ_y/σ_u and A are seen to have an even smaller effect on the correlation of C_{vm}–to–J_Q in comparison with the C_v–to–J_Q correlation, especially for low C_{vm}. When predicting a fracture toughness for the sake of assessing the limit state associated with the onset of stable ductile crack propagation using alternative tests in situations where direct fracture toughness testing is not an option, the advice is to use C_{vm} instead of C_v, σ_y/σ_u or A.

6 Recommendation for further work

In this paper, it has been proposed that Charpy-based measures perform better than the tensile test properties for the purpose for incorporating sufficient upper-shelf toughness into design, and a damage-mechanics-based model is used to estimate the relationship between Charpy energy and fracture toughness. However, the relationship obtained in this work is based on a range of properties typical for S690QL steel and involves the assumption of triaxiality independence which less applicable to some steels. Further research is necessary to describe a more general relationship between Charpy energy and fracture toughness for a broader range of steels before the present findings can be translated into industrial practice. This could be done through further damage-mechanics modelling studies with the use of a more nuanced description for the different stress-state dependence, rate dependence and plastic strain hardening behaviours observed across a range of steel grades or through statistical treatment of large datasets of the identified key mechanical test properties.

Furthermore, this paper proposes that imposing a σ_y/σ_u limit is not a useful measure for ensuring sufficient local ductility against fracture in the upper-shelf as assumed in industry practice. This raises the question of discontinuing its current use as a blanket material ductility requirement for high-strength steels and including it only in the design for failure modes (Wong and Walters 2021) in which it plays a role, such as plastic buckling (Wong and Walters 2023). However, the present study has considered only purely ductile fracture, and the role of the σ_y/σ_u in the upper ductile-to-brittle transition, where cleavage fracture might occur after significant ductile tearing, still needs to be considered, due to the potential effects of plastic straining and plastic zone stress redistribution on cleavage fracture (Ruggieri and Dodds 2015; Ruggieri et al. 2015), considering how σ_y/σ_u is correlated to plastic strain hardening behaviour (Section 3.1.3). Further research is necessary to resolve this question because the literature on the upper-transition from the perspective of macroscopic approaches (Lindqvist and Wallin 2019; Walters and Wallin 2013) is sparse relative to the work done for the lower transition, and as for local approaches, significant improvements are necessary and still being developed for combined ductile and cleavage models (e.g. Seo et al. 2025; Tanguy et al. 2005).

Author contributions W.J.W. contributed in the data visualisation, validation, software, methodology, investigation, formal analysis, conceptualisation and writing the original draft. C.W. contributed in supervision, resources, project administration, methodology, funding acquisition, conceptualisation and reviewing and editing the manuscript.

Funding The authors gratefully acknowledge the joint funding provided by the Bureau Veritas Marine & Offshore SAS, Damen Schelde Naval Shipbuilding BV, Huisman Equipment BV, Lloyd's Register EMEA, POSCO and the Topconsortia voor Kennis en Innovatie (TKI).
The authors also thank Huisman BV for providing the material certificate database used in the study.

Data Availability Statement Data will be made available on request.

Declarations

Competing interests The authors declare no competing interests.

References

AISC (American Institute of Steel Construction), (2022) ANSI/AISC 360–22 Specification for Structural Steel Buildings. AISC, USA

Alabi AA, Moore PL, Wrobel LC et al (2018) Tensile behaviour of S690QL and S960QL under high strain rate. J Constr Steel Res 150:570–580. https://doi.org/10.1016/j.jcsr.2018.08.009

Alexopoulos ND, Tiryakioglu M (2009) Relationship between fracture toughness and tensile properties of A357 cast aluminum alloy. Metallurgical and Materials Transactions a-Physical Metallurgy and Materials Science 40a(3):702–716. https://doi.org/10.1007/s11661-008-9742-8

Algarni M, Bai Y, Choi Y (2015) A study of Inconel 718 dependency on stress triaxiality and Lode angle in plastic deformation and ductile fracture. Eng Fract Mech 147:140–157. https://doi.org/10.1016/j.engfracmech.2015.08.007

ASTM (American Society for Testing and Materials) (2023) E1820–23b Standard Test Method for Measurement of Fracture Toughness. ASTM West Conshohocken. https://doi.org/10.1520/E1820-23B

ASTM (American Society for Testing and Materials) (2024) E8/E8M - 24 Standard Test Methods for Tension Testing of Metallic Materials. ASTM, West Conshohocken

Bai Y, Wierzbicki T (2010) Application of extended Mohr-Coulomb criterion to ductile fracture. Int J Fract 161(1):1–20. https://doi.org/10.1007/s10704-009-9422-8

Banabic D, Aretz H, Paraianu L et al (2005) Application of various FLD modelling approaches. Modell Simul Mater Sci Eng 13(5):759–769. https://doi.org/10.1088/0965-0393/13/5/009

Bao Y, Wierzbicki T (2005) On the cut-off value of negative triaxiality for fracture. Eng Fract Mech 72(7):1049–1069. https://doi.org/10.1016/j.engfracmech.2004.07.011

Besseling JF, van der Giessen E (1994). Mathematical Modelling of Inelastic Deformation. https://doi.org/10.1007/978-1-4899-7186-9

BSI (British Standards Institution), (2019) BS 7910 Guide to methods for assessing the acceptability of flaws in metallic structures. BSI. https://doi.org/10.3403/30369478

Cao TS (2015) Models for ductile damage and fracture prediction in cold bulk metal forming processes: a review. IntJ Mater Form 10(2):139–171. https://doi.org/10.1007/s12289-015-1262-7

CEN (European Committee for Standardization), (2005) EN 1993-1-1 Eurocode 3: Design of steel structures - Part 1–1: General rules and rules for buildings. CEN, Brussels

CEN (European Committee for Standardization), (2019) EN 10025–6 Hot rolled products of structural steels - Part 6: Technical delivery conditions for flat products of high yield strength structural steels in the quenched and tempered condition. CEN, Brussels

CEN (European Committee for Standardization), (2020) prEN 1993-1-1 Draft: Eurocode 3: Design of steel structures - Part 1–1: General rules and rules for buildings. CEN, Brussels

CEN (European Committee for Standardization), (2023) prEN 1993-1-10 Draft: Eurocode 3: Design of steel structures - Part 1–10: Material toughness and through-thickness properties. CEN, Brussels

Chaouadi R, Fabry A (2002) On the utilization of the instrumented Charpy impact test for characterizing the flow and fracture behavior of reactor pressure vessel steels, vol 30, Elsevier, pp 103–117. https://doi.org/10.1016/S1566-1369(02)80011-5

Chaouadi R, Gérard R (2021) Development of a method for extracting fracture toughness from instrumented Charpy impact tests in the ductile and transition regimes. Theoret Appl Fract Mech 115. https://doi.org/10.1016/j.tafmec.2021.103080

Chatterjee S (2020) A new coefficient of correlation. J Am Stat Assoc 116(536):2009–2022. https://doi.org/10.1080/01621459.2020.1758115

Chen A, Zhang P, Chen B et al (2023) A new ductile fracture model for Q460C high-strength structural steel under monotonic loading: Experimental and numerical investigation. Eng Fract Mech 288. https://doi.org/10.1016/j.engfracmech.2023.109358

Clausing DP (1970) Effect of plastic strain state on ductility and toughness. Int J FractMech 6(1):71–85. https://doi.org/10.1007/bf00183662

Considère A (1885) Mémoire sur l'emploi du fer et de l'acier. Annales des Ponts et Chaussées 9:574–775

Cowper GR, Symonds PS (1957) Strain hardening and strain-rate effects in the impact loading of cantilever beams. Tech. Rep. no. 28, Office of Naval Research

Dey S, Borvik T, Hopperstad OS et al (2004) The effect of target strength on the perforation of steel plates using three different projectile nose shapes. Int J Impact Eng 30(8–9):1005–1038. https://doi.org/10.1016/j.ijimpeng.2004.06.004

Dhalla AK, Winter G (1974) Suggested steel ductility requirements. J Struct Div 100(2):445–462. https://doi.org/10.1061/jsdeag.0003717

DNV (Det Norske Veritas) (2021) DNV-RU-SHIP Pt.2 Ch.2. Rules for classification: Ships: Part 2 Materials and welding 2 Metallic materials. DNV

Dong J, Elchalakani M, Li D, et al (2022) Dynamic hardening behavior and ductile fracture of high-strength steel at intermediate strain rates. Journal of Structural Engineering 148(9). https://doi.org/10.1061/(asce)st.1943-541x.0003416

DS Simulia (Dassault Systèèmes Simulia) (2022) ABAQUS 2022. Commercial Finite Element Software

Eason ED, Nelson EE (1989) Improved model for predicting J-R curves from charpy data. Tech. rep., U.S. Nuclear Regulatory Commission

Eason ED, Wright JE, Nelson EE (1991) Multivariable modeling of pressure vessel and piping J-R data. Tech. rep., U.S. Nuclear Regulatory Commission

Fabry A, Walle E, Chaouadi R, et al (1993) RPV steel embrittlement: Damage modeling and micro-mechanics in an engineering perspective. In: AEA/OECD Specialists Meeting on Irradiation embrittlement and optimisation of annealing, https://inis.iaea.org/records/3ny9g-49b74

Feldmann M, Schaffrath S (2017) Assessing the net section resistance and ductility requirements of EN 1993-1-1 and EN 1993-1-12. Steel Construction 10(4):354–364

Feldmann M, Schaffrath S, Sandro C (2020) Draft: Background document to Eurocode 3 EN 1993 – part 1–10: Material toughness - approach for upper-shelf toughness requirements for the design of steel structures based on damage mechanics. Institute of Steel Construction RWTH Aachen University, Tech. rep

Feldmann M, Meissner M, Bartsch H et al (2023) Stand der Untersuchungen zu Werkstoffanforderungen hochfester Stähle S700 bis S960 – FOSTA-Forschungsverbund HOCHFEST. Stahlbau 92(8):468–483. https://doi.org/10.1002/stab.202300033

Gioielli P, Landes J, Paris P, et al (2000) Method for Predicting J-R Curves from Charpy Impact Energy, ASTM, West Conshohocken, PA, pp 61–68. https://doi.org/10.1520/STP13395S

Hirth JP, Froes FH (1977) Interrelations between fracture toughness and other mechanical-properties in titanium-alloys. Metallurgical Transactions a-Physical Metallurgy and Materials Science 8(7):1165–1176. https://doi.org/10.1007/Bf02667402

Hollomon JHJ (1945) Tensile deformation. Transactions of the Metallurgical Society of AIME 162:268–290

Huo JS, Zeng X, Wang HT (2022) Tensile behaviour of TMCP Q690D high-strength structural steel at strain rates from 0.00025 to 760 s-1. Advanced Steel Construction 18(1):488–494. https://doi.org/10.18057/IJASC.2022.18.1.7

IACS (International Association of Classification Societies) (2023) IACS UR W Requirements concerning material and welding. IACS

ISO (International Organization for Standardization) (2019) ISO 6892–1 Metallic materials - Tensile testing - Part 1: Method of test at room temperature. ISO, Geneva

Johnson GR, Cook WH (1985) Fracture characteristics of three metals subjected to various strains, strain rates, temperatures and pressures. Eng Fract Mech 21(1):31–48. https://doi.org/10.1016/0013-7944(85)90052-9

Kussmaul K, Roos E (1985) Statistical evaluation of post-yield fracture mechanics properties on the basis of the notched bar impact test. Nucl Eng Des 87:123–137. https://doi.org/10.1016/0029-5493(85)90101-3

Langenberg P, Nießen T, Dahl W (2000) Bruch- und verformungsverhalten von hochfesten stählen mit streckgrenzen von 690 bis 890 MPa. Stahlbau 69(4):283–291. https://doi.org/10.1002/stab.200000860

Li HF, Wei JL, Yang SP et al (2022) The relationship between fracture toughness and tensile property in high-strength steels. Eng Fail Anal 131. https://doi.org/10.1016/j.engfailanal.2021.105854

Li Y, Wierzbicki T (2010) Prediction of plane strain fracture of AHSS sheets with post-initiation softening. Int J Solids Struct 47(17):2316–2327. https://doi.org/10.1016/j.ijsolstr.2010.04.028

Lindqvist S, Wallin K (2019) Master curve procedure accounting for the combined, constraint, ductile tearing and loading rate effects. Proceedings of the ASME Pressure Vessels and Piping Conference, 2019, Vol 6a https://doi.org/10.1115/PVP2019-93844

LR (Lloyd's Register), (2024) LR-RU-002 Rules for the Manufacture. Testing and Certification of Materials, LR, London

Lu C, Michal G, Venton P (2015) A new fracture velocity model for high grade gas pipelines. In: 20th Joint Technical Meeting on Pipeline Research

Merkle JG, Johnson RE (1985) Example calculations illustrating methods for analyzing ductile flaw stability in nuclear pressure vessels. Int J Press Vessels Pip 18(1):35–53. https://doi.org/10.1016/0308-0161(85)90025-0

Meyers MA (1994) Dynamic Behavior of Materials. John Wiley & Sons Inchttps://doi.org/10.1002/9780470172278

Nonn A, Paredes M, Keim V, (2018) Comparison of fracture models to quantify the effects of material plasticity on the ductile fracture propagation in pipelines. In, et al (2018) 12th International Pipeline Conference, vol Volume 3: Operations, Monitoring, and Maintenance. Materials and Joining ASME. https://doi.org/10.1115/IPC2018-78366

Ruggieri C, Dodds RH (2015) An engineering methodology for constraint corrections of elastic–plastic fracture toughness – part i: A review on probabilistic models and exploration of plastic strain effects. Eng Fract Mech 134:368–390. https://doi.org/10.1016/j.engfracmech.2014.12.015

Ruggieri C, Savioli RG, Dodds RH (2015) An engineering methodology for constraint corrections of elastic–plastic fracture toughness – part ii: Effects of specimen geometry and plastic strain on cleavage fracture predictions. Eng Fract Mech 146:185–209. https://doi.org/10.1016/j.engfracmech.2015.06.087

Sakonder C, Xue L, Paredes M et al (2022) Directional dependence of critical axial strain in X65 pipeline steel subject to combined internal pressure and bending loading. Int J Press Vessels Pip 196. https://doi.org/10.1016/j.ijpvp.2022.104610

Sarzosa DFB, Paredes M, Savioli R et al (2022) Experimental and numerical study on the ductile fracture response of X65 girth-welded joint made of Inconel 625 alloy. Theoret Appl Fract Mech 121. https://doi.org/10.1016/j.tafmec.2022.103533

Schindler HJ (2001) Abschätzung von Bruchzähigkeitskennwerten aus der Bruch- oder Kerbschlagarbeit. Materialwiss Werkstofftech 32(6):544–551. https://doi.org/10.

1002/1521-4052(200106)32:6<544::Aid-mawe544>3.0.Co;2-k

Sedlacek G, Feldmann M, Kühn B et al (2008) Commentary and worked examples to en 1993-1-10 "material toughness and through thickness properties" and other toughness oriented rules in en 1993 - background documents in support to the implementation, harmonization and further development of the eurocodes. Tech. rep, European Commission Joint Research Centre

Seo KW, Kim JY, Kim YJ et al (2024) Finite element ductile fracture simulation of Charpy and drop weight tear tests for API X52. Theoret Appl Fract Mech 133. https://doi.org/10.1016/j.tafmec.2024.104629

Seo KW, Kim JY, Kim YJ et al (2025) Combined ductile-brittle fracture simulation of API X80 under impact loading. Journal of Pipeline Science and Engineering. https://doi.org/10.1016/j.jpse.2025.100295

Shashank Dutt B, Nani Babu M, Ganesan V et al (2025) Prediction of fracture resistance from tensile properties and validation with experimental data for 316 type stainless steels. J Mater Eng Perform 34(2):1526–1539. https://doi.org/10.1007/s11665-024-09140-z

Sreenivasan PR (2014) Estimation of quasi-static J-R curves from Charpy energy and adaptation to ASTM E 1921 reference temperature estimation of ferritic steels. Nucl Eng Des 269:125–129. https://doi.org/10.1016/j.nucengdes.2013.08.017

Studer P, Taras A (2023) Strain-hardening dependent cross-sectional slenderness limits for the plastic resistance of steel beams. J Constr Steel Res 205. https://doi.org/10.1016/j.jcsr.2023.107879

Swift HW (1952) Plastic instability under plane stress. J Mech Phys Solids 1:1–16

Tanguy B, Besson J, Piques R et al (2005) Ductile to brittle transition of an A508 steel characterized by charpy impact test. Eng Fract Mech 72(3):413–434. https://doi.org/10.1016/j.engfracmech.2004.03.011

Taylor GI, Quinney H (1933) The latent energy remaining in a metal after cold working. Proceedings of the Royal Society of London Series A Containing Papers of a Mathematical and Physical Character 143(849):307–326. https://doi.org/10.1098/rspa.1934.0004

Wallin K (1995) Proposal for unified rules for selection of Charpy toughness criteria for both low and extra high strength steels. IIW document X-1318-95

Wallin K (2001) Low-cost J-R curve estimation based on CVN upper shelf energy. Fatigue & Fracture of Engineering Materials & Structures 24(8):537–549. https://doi.org/10.1046/j.1460-2695.2001.00405.x

Wallin K (2021) Critical assessment of the Rolfe-Novak CVN-KIC upper shelf correlation. Eng Fract Mech 258. https://doi.org/10.1016/j.engfracmech.2021.108117

Walters CL, Wallin K (2013) The use of surface appearance in combination with charpy impact energy to determine j-integral values. In: ASME 2013 32nd International Conference on Ocean, Offshore and Arctic Engineering, https://doi.org/10.1115/omae2013-10379

Wang WM, Sluys LJ, de Borst R (1997) Viscoplasticity for instabilities due to strain softening and strain-rate softening. Int J Numer Meth Eng 40(20):3839–3864. https://doi.org/10.1002/(sici)1097-0207(19971030)40:20<3839::Aid-nme245>3.0.Co;2-6

Wierzbicki T, Bao Y, Lee YW et al (2005) Calibration and evaluation of seven fracture models. Int J Mech Sci 47(4–5):719–743. https://doi.org/10.1016/j.ijmecsci.2005.03.003

Wong WJ, Walters CL (2021) Failure modes and rules related to the yield-to-tensile strength ratio in steel structures. In: ASME 2021 40th International Conference on Ocean, Offshore and Arctic Engineering (OMAE). ASME (The American Society of Mechanical Engineers), https://doi.org/10.1115/OMAE2021-61995

Wong WJ, Walters CL (2023) Effect of strain hardening on the rotation capacity of welded I-section high-strength steel beams. Ships and Offshore Structures pp 1–1https://doi.org/10.1080/17445302.2023.2195727

Wong WJ, Walters CL (2024) Effects of strain hardening and the Lode dependence of the fracture strain locus on slant fracture in Charpy V-notch impact testing. In: ASME 2024 43rd International Conference on Ocean, Offshore and Arctic Engineering (OMAE). ASME (The American Society of Mechanical Engineers), https://doi.org/10.1115/OMAE2024-125635

Wong WJ, Walters CL (2025) Damage mechanics model for correlating notch toughness in Charpy impact tests with fracture toughness in cracked static fracture tests. Eng Fract Mech. https://doi.org/10.1016/j.engfracmech.2025.111043

Xue L (2009) Stress based fracture envelope for damage plastic solids. Eng Fract Mech 76(3):419–438. https://doi.org/10.1016/j.engfracmech.2008.11.010

Xue L (2010) Localization conditions and diffused necking for damage plastic solids. Eng Fract Mech 77(8):1275–1297. https://doi.org/10.1016/j.engfracmech.2009.12.008

Yan JB, Liew JYR, Zhang MH et al (2014) Mechanical properties of normal strength mild steel and high strength steel S690 in low temperature relevant to arctic environment. Materials & Design 61:150–159. https://doi.org/10.1016/j.matdes.2014.04.057

Yang X, Yang H, Zhang S (2019) Rate-dependent constitutive models of S690 high-strength structural steel. Constr Build Mater 198:597–607. https://doi.org/10.1016/j.conbuildmat.2018.11.285

Yang X, Yang H, Lai Z et al (2020) Dynamic tensile behavior of S690 high-strength structural steel at intermediate strain rates. J Constr Steel Res 168. https://doi.org/10.1016/j.jcsr.2020.105961

Yun X, Gardner L (2017) Stress-strain curves for hot-rolled steels. J Constr Steel Res 133:36–46

Zhu XK, Leis BN (2005) Influence of yield-to-tensile strength ratio on failure assessment of corroded pipelines. J Pressure Vessel Technol 127(4):436–442